Astronomy & Astrophysics

Three new brown dwarfs and a massive hot Jupiter revealed by TESS around early-type stars[*]

Angelica Psaridi[1] , François Bouchy[1], Monika Lendl[1], Nolan Grieves[1], Keivan G. Stassun[2],
Theron Carmichael[3], Samuel Gill[4,5], Pablo A. Peña Rojas[6], Tianjun Gan[7], Avi Shporer[8], Allyson Bieryla[9],
Rafael Brahm[10,11], Jessie L. Christiansen[12], Ian J. M. Crossfield[13], Franck Galland[1,16], Matthew J. Hooton[14],
Jon M. Jenkins[15], James S. Jenkins[6,17], David W. Latham[18], Michael B. Lund[12], Joseph E. Rodriguez[19],
Eric B. Ting[15], Stéphane Udry[1], Solène Ulmer-Moll[1], Robert A. Wittenmyer[20], Yanzhe Zhang[13], George Zhou[18],
Brett Addison[20], Marion Cointepas[1,16], Karen A. Collins[21], Kevin I. Collins[22], Adrien Deline[1],
Courtney D. Dressing[23], Phil Evans[24], Steven Giacalone[23], Alexis Heitzmann[20], Ismael Mireles[25], Dany Mounzer[1],
Jon Otegi[1,26], Don J. Radford[27], Alexander Rudat[8], Joshua E. Schlieder[28], Richard P. Schwarz[29], Gregor Srdoc[30],
Chris Stockdale[31], Olga Suarez[32], Duncan J. Wright[20], and Yinan Zhao[1]

(Affiliations can be found after the references)

ABSTRACT

Context. The detection and characterization of exoplanets and brown dwarfs around massive AF-type stars is essential to investigate and constrain the impact of stellar mass on planet properties. However, such targets are still poorly explored in radial velocity (RV) surveys because they only feature a small number of stellar lines and those are usually broadened and blended by stellar rotation as well as stellar jitter. As a result, the available information about the formation and evolution of planets and brown dwarfs around hot stars is limited.

Aims. We aim to increase the sample and precisely measure the masses and eccentricities of giant planets and brown dwarfs transiting early-type stars detected by the Transiting Exoplanet Survey Satellite (TESS).

Methods. We followed bright ($V < 12$ mag) stars with $T_{\rm eff} > 6200$ K that host giant companions ($R > 7\,R_\oplus$) using ground-based photometric observations as well as high precision radial velocity measurements from the CORALIE, CHIRON, TRES, FEROS, and MINERVA-Australis spectrographs.

Results. In the context of the search for exoplanets and brown dwarfs around early-type stars, we present the discovery of three brown dwarf companions, TOI-629b, TOI-1982b, and TOI-2543b, and one massive planet, TOI-1107b. From the joint analysis of TESS and ground-based photometry in combination with high precision radial velocity measurements, we find the brown dwarfs have masses between 66 and 68 $M_{\rm Jup}$, periods between 7.54 and 17.17 days, and radii between 0.95 and 1.11 $R_{\rm Jup}$. The hot Jupiter TOI-1107b has an orbital period of 4.08 days, a radius of 1.30 $R_{\rm Jup}$, and a mass of 3.35 $M_{\rm Jup}$. As a by-product of this program, we identified four low-mass eclipsing components (TOI-288b, TOI-446b, TOI-478b, and TOI-764b).

Conclusions. Both TOI-1107b and TOI-1982b present an anomalously inflated radius with respect to the age of these systems. TOI-629 is among the hottest stars with a known transiting brown dwarf. TOI-629b and TOI-1982b are among the most eccentric brown dwarfs. The massive planet and the three brown dwarfs add to the growing population of well-characterized giant planets and brown dwarfs transiting AF-type stars and they reduce the apparent paucity.

Key words. brown dwarfs – planetary systems – techniques: photometric – techniques: radial velocities – stars: early-type – binaries: eclipsing

1. Introduction

Even though our understanding of giant planet formation and evolution mechanisms has significantly improved over the past 20 yr, the impact of the host star's properties (mass, temperature, age, and metallicity) on the giant planet distribution remains to be thoroughly studied. The timescales and occurrences of the different planet formation scenarios have to be assessed, quantified, and compared. To that extent, detecting hot Jupiters and brown dwarfs orbiting hot stars is essential if we want to constrain giant planet and brown dwarf formation models across various stellar types. Since the discovery of the first exoplanet around a solar-like star in 1995 (Mayor & Queloz 1995), more than 500 planets with well-constrained densities ($\sigma_{\rm M}/{\rm M} \leq 25\%$ and $\sigma_{\rm R}/{\rm R} \leq 8\%$) have been discovered by transit surveys and validated with radial-velocity (RV) follow-up, according to the PlanetS exoplanet catalog of Otegi et al. (2020) with accurate mass and radius determinations (accessible on the Data & Analysis Center for Exoplanet DACE[1]). These surveys have mainly focused on late-type main-sequence stars because planets transiting hot and usually fast-rotating stars are harder to validate.

---

[1] https://dace.unige.ch

With effective temperatures higher than 6200 K (Kraft break, Kraft 1967), these stars have thin convective envelopes that do not efficiently generate magnetic winds and drive angular momentum loss. As a result, they remain rapidly rotating and due to their high temperature they exhibit fewer spectral lines. Their high rotation velocities lead to a substantial broadening of their observed spectral lines, making RV measurements of hot stars difficult. In addition, stellar activity and pulsations can induce RV variations that can mask or even mimic the RV signature of orbiting exoplanets (Vanderburg et al. 2016). In particular, only 20% (99 exoplanets) of transiting exoplanets with precise densities have been detected to orbit AF-type stars with T_{eff} >6200 K (≲F8V). Figure 1 summarizes the scarcity of planets detected around host stars with different stellar types. The vertical line at 6200 K indicates the Kraft break where stars retain their high rotational velocities.

Several spectroscopic surveys on volume-limited samples of early-type stars have been performed using the Fourier inter-spectrum method (Chelli 2000), with various spectrographs: the ELODIE (Baranne et al. 1996) survey (Galland et al. 2005b, 2005a, 2006), the SOPHIE (Bouchy & The Sophie Team 2006) survey (Desort et al. 2009, Borgniet et al. 2014, 2019) and the HARPS (Pepe et al. 2002) survey (Desort et al. 2008, Borgniet et al. 2017) have led to several discoveries of planets around F-type stars. In this frame, a planet was also discovered around the A5V-type star β Pictoris (Lagrange et al. 2020). Other interesting detections occurred from transit surveys, such as KELT-9b (Gaudi et al. 2017), MASCARA-1b (Talens et al. 2017), MASCARA-4b (Dorval et al. 2020), WASP-33b (Collier Cameron et al. 2010), and WASP-167b/KELT-13b (Temple et al. 2017). Studying this population is scientifically valuable for several reasons. First, planets orbiting hot stars have a higher probability of being in a misaligned polar or retrograde orbit (Winn et al. 2010). The high obliquities of these planets may shed light on their formation since it can be linked to orbital migration processes around stars of high masses (Fabrycky & Tremaine 2007). Atmospheric characterization of these misaligned hot Jupiters provides constraints on the composition of their atmospheres which may in turn reveal clues as to their formation history. Second, these planets receive large amounts of UV radiation, compared to planets around late-type stars, that can drive unique chemical processes in their atmospheres (Casewell et al. 2015). Third, the core-accretion planet formation scenario predicts an increase in gas giant frequency with stellar mass (Kennedy & Kenyon 2008), therefore enlarging the population of exoplanets transiting massive stars will allow to test such correlation.

The Transiting Exoplanet Survey Satellite (TESS, Ricker et al. 2015) is an all-sky survey that has been monitoring bright targets for more than 3 yr. Unlike Kepler, TESS is optimized for bright stars and was designed to search for planets transiting a large variety of stars including early-type, massive stars. TESS has contributed tens of new planets (e.g., TOI-1431b/MASCARA-5b; Addison et al. 2021, TOI-2109b; Wong et al. 2021, TOI-2685b; Jones et al. 2019, TOI-3362b; Dong et al. 2021) to this still sparse population and more than 300 candidates released as TESS Objects of Interest (TOIs).

We performed a RV follow-up dedicated to the validation and mass measurement of extrasolar planets and brown dwarfs transiting a sample of AF-type, main-sequence stars from the TESS mission and we present the discovery of TOI-1107b, TOI-629b, TOI-1982b, and TOI-2543b, a massive planet and three massive brown dwarfs, respectively. TOI-1107b, TOI-1982b, and TOI-2543 orbit F-type stars while TOI-629b orbits a T_{eff} =
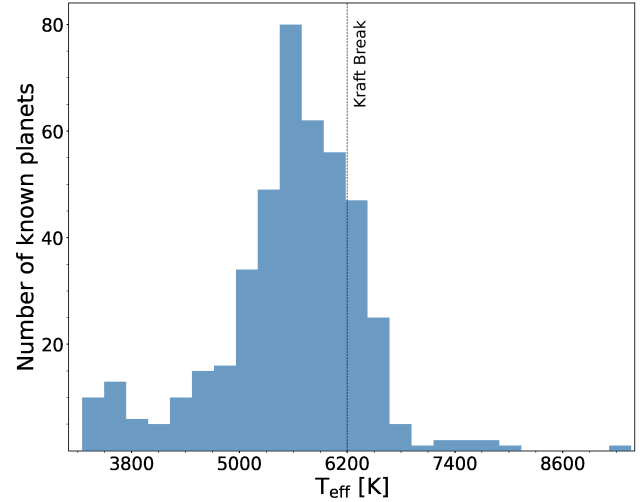
Fig. 1. Number of known exoplanets from the PlanetS Catalog (Otegi et al. 2020, accessible on the Data & Analysis Center for Exoplanet DACE[1]) with precise mass and radius measurements ($\sigma_M/M \leq 25\%$ and $\sigma_R/R \leq 8\%$) as a function of stellar effective temperature. The black vertical line at 6200 K indicates the Kraft break (Kraft 1967).

9110 ± 200 K, A-type star. In Sect. 2, we describe our sample, the TESS photometric data and the ground-based follow-up photometric and spectroscopic observations. Section 3 presents the host star characterization and the global photometric and spectroscopic analysis of the systems. We discuss the systems in context in Sect. 4 and conclude in Sect. 5. As a by-product of our RV follow-up, we present four low-mass eclipsing components in the Appendix C.

2. Observations

2.1. Sample selection and observations

We carried out a RV follow-up focusing on TOIs with spectral types between A0 and ~F8. The F8 (~6200 K) limit corresponds to the Kraft break and the A0 to the earliest spectral type for which the cross-correlation technique with the appropriate binary mask provides precise RV measurements. The sample consists of 312 TESS giant planet candidates ($R > 7 R_\oplus$) brighter than $V = 12$ mag that were detected during the first 3 yr of the TESS mission (Sectors 1–39). We exclude targets photometrically identified as false positives (transit depth chromaticity measured in different filters) such as blended eclipsing binaries (BEB), spectroscopically identified as false positives such as single- and double-lined spectral binaries (SB1 and SB2) and BEBs and already known planets. Our final sample consists of ~120 targets. Thanks to this survey, we confirm the discovery of three new brown dwarfs (TOI-629b, TOI-1982b, and TOI-2543b), a massive planet (TOI-1107b) and four low-mass stars (identified as SB1s). The list and the parameters of the identified SB1 systems can be found in the Appendix C.

2.2. TESS and ground-based photometry

All four targets were initially observed and detected by the NASA TESS space mission. Afterward, ground-based time-series follow-up photometry was performed for TOI-1107 and TOI-1982 as part of the TESS Follow-up Observing Program (TFOP, Collins et al. 2018) to confirm the TESS photometric

Table 1. Summary of the TESS and ground photometric observations of TOI-1107, TOI-629, TOI-1982 and TOI-2543.

Date(s)	Facility	Detrending
TOI-1107		
2021 Apr. 28–Jun. 24	TESS 2-min	GPs
2019 Apr. 22–Jul. 18	TESS FFI	GPs
2020 May. 07	Brierfield (B)	$p(t)$, $p(sky)$ & $p(AM)$
2020 Aug. 13	ASTEP (R_c)	$p(t)$ & $p(AM^2)$
2021 Mar. 25	LCO-SAAO (B)	$p(sky)$, $p(FWHM)$ & $p(AM)$
2021 Mar. 25	LCO-SAAO (z')	$p(FWHM)$
TOI-629		
2020 Dec. 18–2021 Jan. 13	TESS 2-min	GPs
2018 Dec. 11–2019 Jan. 07	TESS FFI	GPs
TOI-1982		
2021 Apr. 02–Apr. 28	TESS 2-min	GPs
2019 Apr. 22–May. 21	TESS FFI	GPs
2020 Jul. 01	Hazelwood (R_c)	$p(sky)$ & $p(FWHM)$
2021 Apr. 02	El Sauce (R_c)	$p(sky)$ & $p(AM)$
2021 Apr. 19	LCO-CTIO (B)	$p(sky)$ & $p(AM)$
2021 Apr. 19	LCO-CTIO (z')	$p(sky)$ & $p(AM)$
TOI-2543		
2021 Jan. 13–Feb. 09	TESS 2-min	–
2019 Feb. 02–Feb. 28	TESS FFI	GPs

Notes: The notation of the baseline models for, $p(j^i)$, refers to a polynomial of degree i in parameter j (t:time, AM:airmass, FWHM:stellar FWHM and sky:sky background). The notation of GPs refers to Gaussian Processes. The low level of correlated noise in TOI-2543 2-min cadence light curves did not necessitate further detrending.

ephemerides and exclude blending scenarios. The summary of the observations can be found in Table 1 and their description below. All light curves can be found in the Appendix A.

2.2.1. TESS light curves

The transit signatures were initially detected by TESS during the first year of the survey (July 2018–July 2019) in the Full Frame Image (FFI) observations with a cadence of 30 min and flagged as promising TOIs for follow-up observations. Afterward, they were reobserved at 2-min cadence during the third year of the mission (July 2020 – July 2021). The photometry of the short cadence data is extracted by the Science Processing Operations Center (SPOC; Jenkins et al. 2016) and consists of the Simple Aperture Photometry (SAP) flux and the Presearch Data Conditioning SAP (PDCSAP; Smith et al. 2012, Stumpe et al. 2012, 2014) flux. For our analysis, we made use of the PDCSAP light curves since they are corrected for long term systematic trends, such as instrumental artifacts and dilution. The observations at 30-min cadence were processed by the MIT Quick Look Pipeline (QLP; Huang et al. 2020). When visually comparing the various light curves, we noticed that the detrended QLP light curves showed a slighly increased flux during transit compared to the un-detrended data. Therefore, we decided to use the raw normalized simple aperture photometry from the best aperture (SAP flux) and account for systematic noise using Gaussian Process regression. All data are publicly available and were downloaded from the Mikulski Archive for Space Telescopes (MAST[2]).

TOI-1107 (TIC 394561119) was observed in Sectors 11–13 with 30-min cadence and Sectors 38 and 39 with 2-min cadence.

---

[2] http://archive.stsci.edu/tess/

We detected 17 transits in the FFIs and 13 transits in 2-min cadence light curves with a transit depth of ~0.54% and an average period of 4.08 days. TOI-1107 passed all the Data Validation (DV) tests (Twicken et al. 2018, Li et al. 2019) and the difference image centroiding test that placed the transit signature source within $0.2 \pm 2.5''$ of the target star.

TOI-629 (TIC 293853437) was monitored in Sector 6 at 30-min and Sector 33 at 2-min cadence. Three transits with a depth of ~0.23% and a period of 8.72 days were identified in both QLP and 2-min data. The candidate passed the DV test and the difference image centroid test located the source of the transits to within $2.0 \pm 2.5''$ of the target star.

TOI-1982 (TIC 437329044) was observed in Sector 11 at 30-min and Sector 37 at 2-min cadence. The 30-min cadence data were processed by the QLP that identified two ~0.53% deep transits 17.1 days apart located at the beginning and at the end of the light curve. During perigee passage while downloading data, the data collection was paused for 1.18 days near the middle of Sector 11. As a result, the period of the target was initially reported to be half (8.58 days). Later, the 2-min cadence data confirmed the 17.1 days period with only one transit visible in Sector 37.

Finally, TOI-2543 (TIC 270604417) was observed in Sector 8 at 30-min cadence and in Sector 34 at 2-min cadence. Two transits were detected in the QLP data and three transits in the 2-min data with a depth of ~0.28% and an orbital period of 7.54 days. The transit signature passed the DV test and the difference image report located the source of the transits to within $0.8 \pm 2.5''$ of the target star.

The Target Pixel Files (TPFs) of our targets and the aperture masks used by the pipeline to extract the photometry (orange pixels), generated with `tpfplotter`, can be found in Fig. 2. The position of nearby stars from the *Gaia* DR2 catalog is marked with red circles. The size of the red circles indicates the different magnitudes in contrast with the target star that is marked with a white cross. For TOI-629, TOI-1982 and TOI-2543 no nearby sources are identified within 6 mag of the target in the aperture mask. For TOI-1107, we identified one star within the aperture at an angular distance of 43.69″ and with magnitude contrast $\Delta m = 5.6$ mag in the G-band. The complementary ground-based seeing-limited photometry with several instruments (see Table 1) confirms that the signal originates from TOI-1107. Moreover, PDCSAP flux light curves account for the dilution caused by nearby stars in order to prevent underestimation of the transiting object radius. For TOI-1107, the estimated flux contamination ratio (ratio of the total contaminant flux over the target star flux in TESS-band) is 0.01.

2.2.2. LCOGT photometric follow-up

We observed full transits of TOI-1107b in B-band and Pan-STARRS z-short band on March 25, 2021 from the Las Cumbres Observatory Global Telescope (LCOGT; Brown et al. 2013) 1.0-m network node at South Africa Astronomical Observatory (SAAO). We observed ingresses of TOI-1982b in B-band and Pan-STARRS z-short band on April 19, 2021 from the LCOGT 1.0-m network node at Cerro Tololo Inter-American Observatory (CTIO). The data that are affected by poor sky transparency have been removed from the light curves. We use the `TESS Transit Finder`, which is a customized version of the `Tapir` software package (Jensen 2013), to schedule our transit observations. The 1.0-m telescopes are equipped with 4096×4096 SINISTRO cameras having an image scale of 0.389″ per pixel, resulting
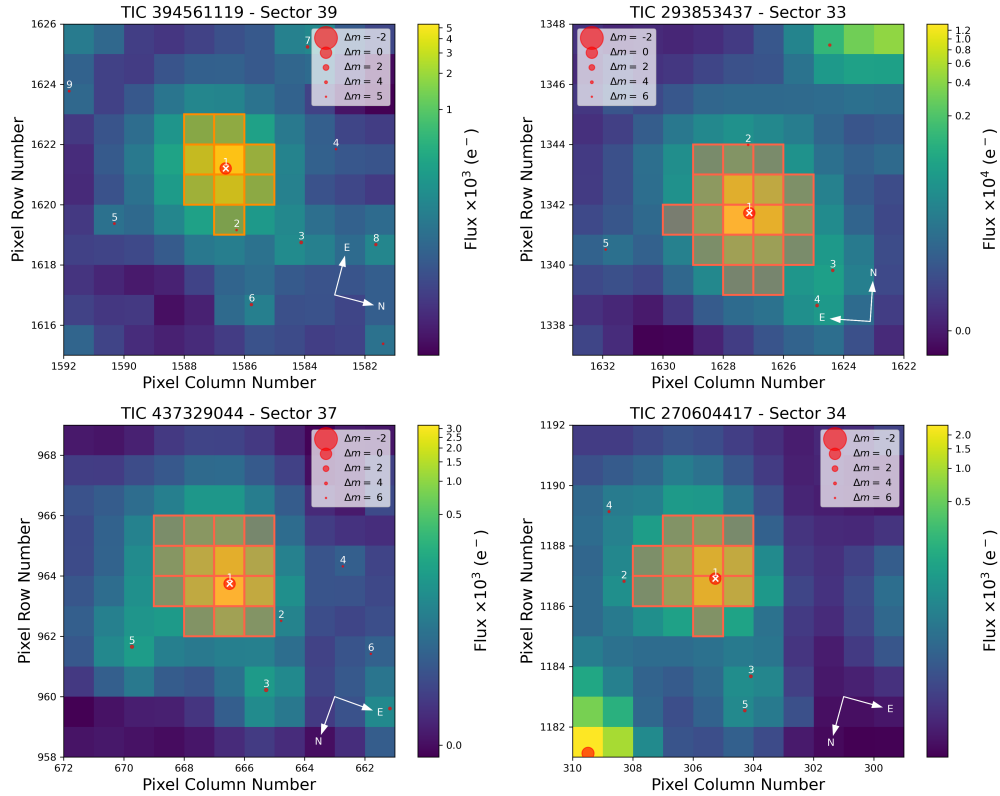
Fig. 2. TESS Target Pixel File (TPF) of TOI-1107 (TIC 394561119; *top left*), TOI-629 (TIC 293853437; *top right*), TOI-1982 (TIC 437329044; *bottom left*), and TOI-2543 (TIC 270604417; *bottom right*) created with `tpfplotter` (Aller et al. 2020). Orange pixels define the aperture mask that was used to extract the photometry. Red circles indicate the neighbor *Gaia* DR2 catalog objects. The size is proportional to the brightness difference of the sources with the targets (see legend). Our targets are marked with a white cross. Pixel scale is 21″ pixel^{-1}.

in a $26' \times 26'$ field of view. The images were calibrated by the standard LCOGT `BANZAI` pipeline (McCully et al. 2018), and photometric data were extracted using `AstroImageJ` (Collins et al. 2017). The images were focused and have mean stellar point-spread-functions with a FWHM of ~2″, and circular photometric apertures with radius 3.9″ (SAAO) and 5.8″ (CTIO) were used to extract the differential photometry. A larger aperture was used for the CTIO observations due to the poor skies and highly variable seeing. The photometric apertures exclude all flux from the nearest *Gaia* EDR3 neighbors. Achromatic transits were detected on-target in both systems.

2.2.3. Hazelwood photometric follow-up

The Hazelwood Observatory is a private backyard observatory with a 0.32-m Planewave CDK telescope working at $f/8$, a SBIG STT3200 2148×1472 CCD, giving a $20' \times 13'$ field of view and 0.55″. The Hazelwood Observatory, operated by Chris Stockdale in Victoria, Australia, observed a 13 ppt egress of TOI-1982 in R_c filter on July 01, 2020 and checked all nearby stars confirming that none of them show an eclipse that could explain the transit seen in TESS data.

2.2.4. El Sauce photometric follow-up

We observed a full transit of TOI-1982 on April 02, 2021 in Johnson-Cousins R_c-band using the Evans 0.36-m telescope at El Sauce Observatory in Coquimbo Province, Chile. The telescope is equipped with a STT1603-3 CCD camera with 1536×1024 pixels binned 2×2 in-camera resulting in an image

scale of 1.47″ pixel^{-1}. The photometric data for TOI-1982 were obtained from 455×60 sec exposures using a circular 8.8″ aperture, processed in AstroImageJ (Collins et al. 2017).

2.2.5. ASTEP photometric follow-up

TOI-1107 was observed on August 13, 2020, with the Antarctica Search for Transiting ExoPlanets (ASTEP) program on the East Antarctic plateau at a latitude of −75.1 deg and elevation of 3233 m (Guillot et al. 2015; Mékarnia et al. 2016). ASTEP is a custom 0.4 m Newtonian telescope equipped with a 5-lens Wynne coma corrector and a 4k × 4k front-illuminated FLI Proline KAF-16801E CCD. The camera has an image scale of 0.93″ pixel^{-1} resulting in a $1° \times 1°$ corrected field of view. The focal instrument dichroic plate splits the beam into a blue wavelength channel for guiding, and a nonfiltered red science channel roughly matching an R_c transmission curve (Abe et al. 2013). The telescope is automated or remotely operated when needed. Due to the extremely low data transmission rate at the Concordia Station, the data are processed on-site using an automated IDL-based aperture photometry pipeline. The calibrated light curve is reported via email and the raw light curves of about 1000 stars of the field are transferred to Europe on a server in Rome, Italy and are then available for deeper analysis. These data files contain each star's flux computed through 10 fixed circular apertures radii, so that optimal light curves can be extracted. For TOI-1107, an 11.2 pixel radius aperture gave the best result. TOI-1107 was observed under good weather conditions with a non-windy (~3 m s^{-1}) clear sky, and air temperatures ranged between −65°C and −75°C.
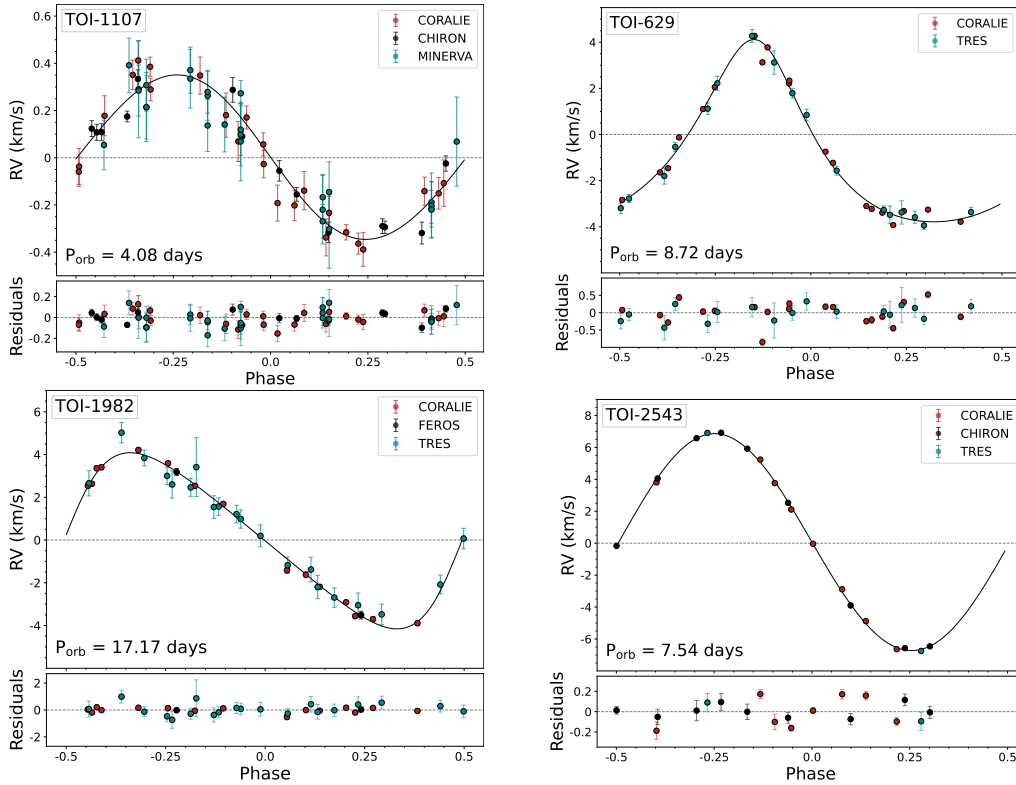
Fig. 3. Relative RVs of TOI-1107 (*top left*), TOI-629 (*top right*), TOI-1982 (*bottom left*) and TOI-2543 (*bottom right*). The different colors indicate different instruments. The black line shows the model fit derived with `juliet`. The residuals of the model fit are shown in the bottom panels.

2.2.6. Brierfield photometric follow-up

We observed a transit of TOI-1107 on May 06, 2020 in the *B*-band using a 0.36-m telescope (PlaneWave CDK14) at the Brierfield Observatory, a home observatory in Brierfield, New South Wales, Australia. The detector was a Moravian 16803 camera, which provided a pixel scale of 1.47″ pixel^{-1}. Seeing conditions were average, with a full moon. We observed a continuous transit using 143 images of 180 s each over 558 min. The images were reduced and measured with AstroImageJ using a photometric aperture of 10.29″.

2.3. High resolution spectroscopy

The four targets were monitored with different spectrographs, CORALIE, CHIRON, TRES, FEROS, and MINERVA-Australis, in order to identify the nature of the candidate, determine its mass and measure its orbital parameters. These observations are described in the following paragraphs and the radial velocities are displayed in Fig. 3.

2.3.1. CORALIE

For all the targets we obtained spectroscopic data with the high resolution CORALIE spectrograph that is installed at the Swiss 1.2-m Leonhard Euler Telescope at ESO's La Silla Observatory (Queloz et al. 2001). CORALIE has a resolution of $R \sim 60\,000$ and is fed by a 2″ fiber. A total of 24 RVs were obtained for TOI-1107 from 2021 April 03 to 2021 June 10 using exposure times of 1800 s which translated in spectra with a signal-to-noise ratio per resolution element (S/N) between 15 and 34. TOI-629 was observed 20 times with CORALIE from 2020 November 26 to 2021 March 28 with exposure times of 1800–2400 s resulting in

a S/N between 39 and 65. We collected 15 RVs for TOI-1982 from 2021 April 12 to 2021 June 12 using 1800–2400 s exposures giving a S/N between 15 and 33. Finally, we obtained eight spectra for TOI-2543 from 2021 November 23 to 2021 December 25 using exposure times of 1800 s resulting in a S/N between 13 and 25.

The RV of each epoch was derived by cross-correlating the spectrum with a binary mask that matches the stellar spectral type (Baranne et al. 1996). Afterward, a Gaussian is fit to the cross-correlation function (CCF). The RV measurement of each spectrum corresponds to the central position of the Gaussian fit. The bisector-span (BIS), the contrast (depth) and the full width at half-maximum (FWHM) were recorded with the standard CORALIE data reduction pipeline. For TOI-629, our hottest target, we used an A0 binary mask. The RVs of TOI-1107 and TOI-1982 were computed by cross-correlating with several binary masks and selected a G2 mask (Pepe et al. 2002) that reached higher precision in the mass measurement.

For each star, we also compute the RVs with the Fourier interspectrum method (Chelli 2000), consisting of correlating, in the Fourier space, the spectra of the star with a reference spectrum built by averaging all the spectra acquired for this star (Galland et al. 2005b). The resulting RVs are consistent with those obtained with the CCF method described above.

2.3.2. TRES

We used the TRES instrument on Mt. Hopkins, Arizona, USA to obtain spectra for TOI-629 and TOI-1982. TRES has a resolving power of $R \sim 44\,000$ and covers a wavelength range of 3900 Å to 9100 Å. We used multiple echelle orders within this wavelength range for each spectrum to measure a relative RV at each phase

in the orbit of the transiting BD. We visually review the orders to remove cosmic rays and omit those with low S/N. Each order is cross-correlated with the highest observed signal-to-noise spectrum of the target star and then the average RV of all the orders per spectrum is taken as the RV of the star for that observation. For TOI-629, we took a total of 18 spectra with TRES. These spectra were taken between 2019 September 17 and 2019 October 28 with exposure times ranging between 600 s and 2200 s and S/N between 64 and 165. For TOI-1982, we took a total of 20 spectra with TRES. The first of these spectra was taken on 2021 January 8, but the remaining spectra were taken months later from 2021 April 15 to 2021 June 2. The exposure times for these spectra range from 720 s to 3600 s and a S/N range of 22 to 55. Finally, for TOI-2543, we collected two spectra on 2021 March 22 and on April 2 with exposure times of 1900 s and 2400 s, respectively. The S/N of the spectra is 30 and 38.

2.3.3. CHIRON

TOI-1107 and TOI-2543 were observed with the CHIRON fiber fed echelle spectrograph at the SMARTS 1.5-m telescope located at Cerro Tololo Inter-American Observatory, Chile (Tokovinin et al. 2013). CHIRON is a high resolution echelle, with a resolving power of $R = 80\,000$ and a spectral coverage of 4100–8700 Å. Observations of TOI-2543 were obtained in the *fiber* mode, yielding a spectral resolving power of $R \sim 28\,000$. For TOI-1107, we took a total of 14 spectra from 2021 January 15 to 2021 March 31 with an exposure time of 1800 s and S/N between 20 and 39. A total of 9 RVs were obtained for TOI-2543 from 2021 April 06 to 2021 May 09 using a median exposure time of 1800 s, resulting in a median S/N of ~120. We make use of spectra extracted via the official CHIRON pipeline as per Paredes et al. (2021). Radial velocities were derived from a least-squares deconvolution between the observation and a nonrotating synthetic template, generated using the ATLAS9 atmosphere models (Castelli & Kurucz 2004) at the spectral parameters of the targets. The derived broadening profile is fit with a kernel accounting for the effects of rotational, macroturbulent, and instrumental broadening and radial velocity shift. In addition, we also estimate stellar atmosphere parameters for the targets. We match the observed spectra against a library of ~10 000 observed spectra classified by the Spectroscopic Classification Pipeline (Buchhave et al. 2012). The library is interpolated and the observed spectrum classified via a Gradient Boosting Classifier from the `scikit-learn` package. The uncertainties in our classification is the scatter in the results from each observed epoch, and do not account for systematic uncertainties that may be present in the template matching.

2.3.4. FEROS

We obtained two spectra of TOI-1982 with the Fiber-fed Extended Range Optical Spectrograph (FEROS, $R = 50\,000$) mounted on the MPG 2.2-m telescope installed at La Silla Observatory, in Chile. These two observations were executed on January 28, 2020 and March 07, 2020 close to orbital phases 0.25 and 0.75 according to the photometric ephemeris provided by TESS. The adopted exposure time was of 600 s which translated into a S/N of ~90. These observations were performed with the simultaneous calibration mode using a ThAr lamp in the secondary fiber, which allows to trace some instrumental velocity drifts. FEROS data was processed with the CERES pipeline (Brahm et al. 2017), which performs the optimal extraction,

wavelength calibration and barycentric correction of the raw data. Precision RVs and line bisector spans were also computed with CERES by using the cross-correlation technique.

2.3.5. MINERVA-Australis

We obtained 26 observations of TOI-1107 from 2020 October 29 to 2021 January 30 using the Minerva-Australis telescope array (Addison et al. 2019), located at Mt Kent observatory, Australia. Minerva-Australis is composed of four identical 0.7-m CDK700 telescopes feeding into a single environment controlled KiwiSpec spectrograph. The spectrograph has a resolving power of $R \sim 80\,000$ over the wavelength region of 5000–6300 Å. The adopted exposure time was of 3600 s which translated into a S/N of ~30. Simultaneous wavelength calibration is provided by two additional fibers that bracket the telescope fibers, each illuminated by a quartz lamp through an iodine cell. We optimally extract the spectra from each telescope fiber individually. RVs are measured from each telescope independently via a cross-correlation between individual exposures and a spectral template generated from the median combined observed target star spectra.

2.4. High resolution imaging

TESS's large pixel size (21″) makes it necessary to consider possible flux contamination by nearby stars that can result in flux dilution and therefore underestimation of the observed transit depth or even false-positive transit signals. Stellar neighbors can be ruled out with high angular resolution imaging.

In this work we used speckle imaging with the 4.1-m Southern Astrophysical Research (SOAR) telescope (Tokovinin 2018) to confirm that the periodic signals originate from our targets. SOAR speckle imaging was obtained for three of our four targets in *I*-band, a similar near-IR bandpass as TESS. TOI-1107 was observed on January 08, 2020, TOI-629 on November 11, 2019 and TOI-1982 on July 17, 2021. No nearby sources were detected within 3″. Figure 4 shows the contrast curve with the 5σ detection limit marked with a black line. The inset images zoomed and centered to the targets that represent the speckle auto-correlation function do not show any stellar companions.

We observed TOI-2543 on March 28, 2021 using the ShARCS camera on the Shane 3-m telescope at Lick Observatory (Kupke et al. 2012; Gavel et al. 2014; McGurk et al. 2014). The observation was taken with the Shane adaptive optics system in natural guide star mode. The final image was constructed using a sequence of images taken in a 4-point dither pattern with a separation of 4″ between each dither position. The image at each dither position was taken using a Ks filter ($\lambda_0 = 2.15\,\mu m$, $\Delta\lambda = 0.32\,\mu m$) with an exposure time of 15 s. A more detailed description of the observing strategy and reduction procedure can be found in Savel et al. (2020). Our reduced image and corresponding contrast curve are shown in Fig. 4. We find no nearby stellar companions within our detection limits.

3. Analysis

3.1. Host star analysis

3.1.1. Spectral analysis

In order to determine suitable priors for our later spectral energy distribution (SED) fitting that provides us with the final stellar parameters, we use the CORALIE spectra. Each spectrum was
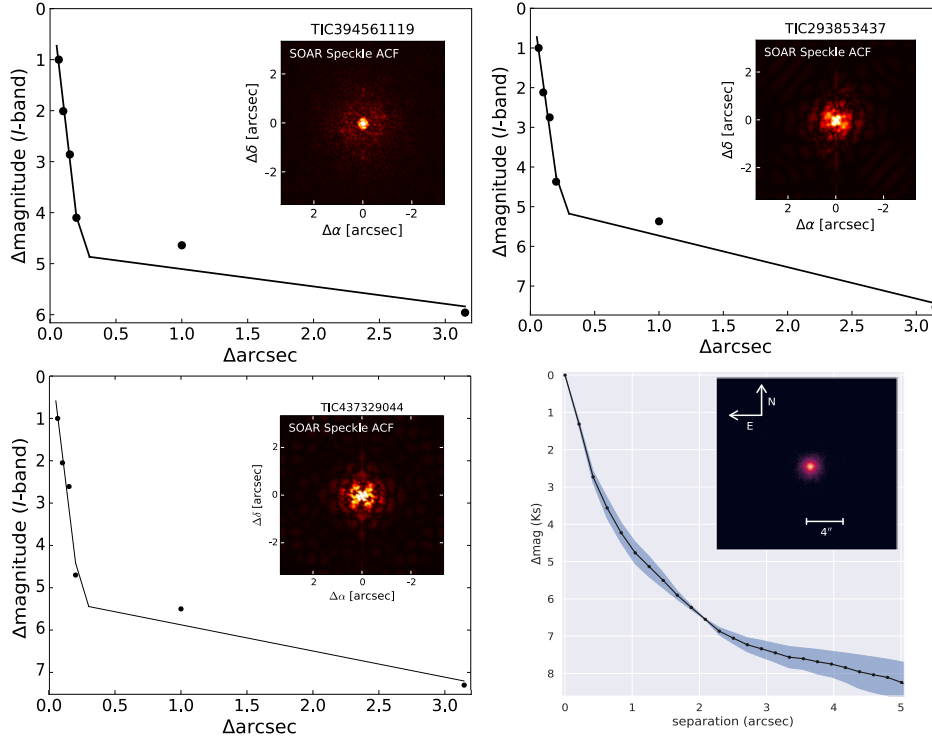
Fig. 4. SOAR speckle imaging (5σ upper limits) of TOI-1107 (TIC 394561119; *top left*), TOI-629 (TIC 293853437; *top right*), and TOI-1982 (TIC 437329044; *bottom left*) that rules out stellar companions within 3″. The image inset represents the speckle auto-correlation function. Adaptive optics image and contrast curve for TOI-2543 (TIC 270604417; *bottom right*) taken with the ShARCS camera on the Shane 3-m telescope at Lick Observatory. The contrast curve was generated by calculating the median values (solid lines) and root-mean-square errors (blue, shaded regions) in annuli centered on the target, where the bin width of each annulus is equal to the full width at half maximum of the point spread function.

shifted to a common wavelength axis and combined to a 1D coadded spectrum to increase the signal-to-noise.

For the stellar characterization of TOI-1107, TOI-1982, and TOI-2543 we use `SpecMatch-Emp` (Yee et al. 2017). `SpecMatch-Emp` is able to extract the fundamental properties of a star, including the effective temperature ($T_{\rm eff}$), surface gravity (log g), and metallicity ([Fe/H]), using its optical spectra. These spectra are compared to a library of 404 high resolution ($R \sim 60\,000$) and high signal-to-noise ($S/N > 100$) stellar spectra obtained with Keck/HIRES. The code is able to achieve accuracies of 100 K in effective temperature, 15% in stellar radius and 0.09 dex in metallicity. In order to match our spectra to the library via χ^2 minimization we use the spectral region from 5100 to 5400 Å that includes the Mgb triplet. For TOI-1107, TOI-1982, and TOI-2543 we ran `SpecMatch-Emp` on 24, 15, and eight stacked CORALIE spectra, respectively. For TOI-2543, TRES spectra are also used to derive stellar parameters using the Stellar Parameter Classification tool (SPC; Buchhave et al. 2012). SPC cross-correlates each observed spectrum against a grid of synthetic spectra based on Kurucz atmospheric model (Kurucz 1992) to determine the stellar effective temperature, surface gravity, metallicity, and rotational velocity. The parameters are in agreement with the CORALIE spectral analysis.

Since `SpecMatch-Emp` is not applicable to stars with effective temperatures higher than ~7000 K, we use a different method to obtain the stellar atmospheric parameters of the A-type star TOI-629. In particular we use the analysis package `iSpec` (Blanco-Cuaresma et al. 2014) to determine the $T_{\rm eff}$, log g_*, and [Fe/H] using the coadded CORALIE spectra for this target. To generate synthetic spectra we use SPECTRUM (Gray & Corbally 1994) which is a radiative transfer code and ATLAS9

model atmospheres (Castelli & Kurucz 2004). We estimate macroturbulence with Equation 5.10 from Doyle et al. (2014) and microturbulence is accounted for at the synthesis stage using Eq. (3.1) from the same source. We estimate the effective temperature $T_{\rm eff}$ and gravity log g_* using the Hα, Ca H, and K lines while other available metals are used to determine [Fe/H] and the projected rotational velocity $v \sin i_*$ (Table 2). We fit trial synthetic model spectra until we reach an acceptable match to the data. For the uncertainties estimation we vary individual parameters until the model spectrum is no longer compatible with the data.

3.1.2. Spectral energy distribution

As an independent check on the derived stellar parameters, we perform an analysis of the broadband spectral energy distribution (SED) together with the *Gaia* eDR3 parallax we determined an empirical measurement of the stellar radius, following the procedures described in Stassun & Torres (2016) and Stassun et al. (2017, 2018). As available, we pulled the $B_T V_T$ magnitudes from *Tycho-2*, the *BVgri* magnitudes from APASS, the JHK_S magnitudes from *2MASS*, the W1–W4 magnitudes from *WISE*, and the *G* magnitude from *Gaia*. We also use the *GALEX* NUV and/or FUV fluxes when available. Together, the available photometry spans the full stellar SED over the wavelength range 0.35–22 μm, and extends down to 0.15 μm when *GALEX* data are available (see Fig. 5). We perform a fit using Kurucz stellar atmosphere models, with the priors on effective temperature ($T_{\rm eff}$), surface gravity (log g), and metallicity ([Fe/H]) from the spectroscopically determined values. The remaining free parameter is the extinction (A_V), which we restrict to the maximum

Table 2. Stellar and companion parameters for TOI-1107, TOI-629, TOI-1982, and TOI-2543 systems.

Property	TOI-1107	TOI-629	TOI-1982	TOI-2543	Source
Identifiers					
TIC ID	394561119	293853437	437329044	270604417	TICv8
2MASS ID	J10222579-8213080	J06231868+0053000	J13502038-2323001	J09062327+0334036	2MASS
Gaia ID	5192364501633274880	3123364264204562944	6287361053627037696	579084083968560256	*Gaia* DR2
Astrometric properties					
R.A. (J2000)	10:22:25.82	06:23:18.69	13:50:20.36	09:06:23.26	*Gaia* DR2
Dec (J2000)	−82:13:07.97	00:53:00.11	−23:23:00.16	03:34:03.61	*Gaia* DR2
Parallax (mas)	3.53 ± 0.03	2.97 ± 0.07	3.72 ± 0.04	2.33 ± 0.18	*Gaia* DR2
Distance (pc)	283.61 ± 2.03	336.29 ± 8.09	268.54 ± 2.87	429.61 ± 33.42	*Gaia* DR2
$\mu_{R.A.}$ (mas yr^{-1})	9.033 ± 0.015	6.521 ± 0.020	-29.579 ± 0.021	-7.922 ± 0.194	*Gaia* DR2
μ_{Dec} (mas yr^{-1})	3.101 ± 0.014	-3.758 ± 0.018	-6.484 ± 0.018	-5.917 ± 0.147	*Gaia* DR2
Photometric properties					
TESS (mag)	10.007 ± 0.006	8.694 ± 0.006	10.192 ± 0.006	10.816 ± 0.006	TICv8
B (mag)	11.038 ± 0.085	8.838 ± 0.036	11.064 ± 0.088	11.718 ± 0.181	Tycho-2
V (mag)	10.553 ± 0.006	8.737 ± 0.003	10.551 ± 0.006	11.178 ± 0.012	Tycho-2
G (mag)	10.377 ± 0.003	8.7320 ± 0.0004	10.5063 ± 0.0005	11.1730 ± 0.0004	*Gaia* DR2
J (mag)	9.545 ± 0.024	8.540 ± 0.037	9.798 ± 0.028	10.280 ± 0.024	2MASS
H (mag)	9.322 ± 0.023	8.607 ± 0.075	9.592 ± 0.022	10.052 ± 0.023	2MASS
K (mag)	9.205 ± 0.019	8.533 ± 0.021	9.54 ± 0.019	10.010 ± 0.023	2MASS
Stellar parameters					
$T_{\rm eff}$ (K)	6311 ± 98	9100 ± 200	6325 ± 110	6060 ± 82	Sect. 3.1.1
$[Fe/H]$ dex	-0.10 ± 0.09	0.10 ± 0.15	-0.10 ± 0.09	-0.28 ± 0.10	Sect. 3.1.1
log g (cgs)	4.05 ± 0.04	4.02 ± 0.05	4.23 ± 0.04	4.01 ± 0.08	Sect. 3.1.1
$v \sin i_*$ (km s^{-1})	12.31 ± 0.79	56.93 ± 3.61	37.58 ± 2.38	8.2 ± 0.5	Sect. 4.3
R_* ($R_\odot$)	1.81 ± 0.06	2.37 ± 0.11	1.51 ± 0.05	1.86 ± 0.15	Sect. 3.1.2
M_* ($M_\odot$)	1.35 ± 0.08	2.16 ± 0.13	1.41 ± 0.08	1.29 ± 0.08	Sect. 3.1.2
Age (Gyr)	$2.6 \pm 0.2^{(*)}$	0.32 ± 0.13	3.6 ± 1.5	5.6 ± 0.9	Sect. 4.3$^{(*)}$, 3.1.2
A_v (mag)	0.20 ± 0.05	0.37 ± 0.05	0.01 ± 0.01	0.02 ± 0.02	Sect. 3.1.2
L_* ($L_\odot$)	4.69 ± 0.43	34.78 ± 4.45	3.29 ± 0.32	4.21 ± 0.72	3.1.2
χ_v^2	1.2	1.2	1.5	0.8	Sect. 3.1.2
F_{bol} (10^{-9} erg s^{-1} cm^{-2})	1.88 ± 0.02	10.61 ± 0.04	1.40 ± 0.02	0.77 ± 0.02	Sect. 3.1.2
$P_{\rm rot}/\sin i_*$ (days)	–	1.77 ± 0.10	–	8.73 ± 0.82	Sect. 3.1.2
Companion parameters					
P (days)	$4.0782387 ^{+0.0000024}_{-0.0000025}$	$8.717993 ^{+0.000012}_{-0.000013}$	$17.172446 ^{+0.000043}_{-0.000044}$	$7.542776 ^{+0.000031}_{-0.000031}$	Sect. 3.2
$p = R_b/R_*$	$0.07379 ^{+0.00033}_{-0.00030}$	$0.04790 ^{+0.00043}_{-0.00042}$	$0.06914 ^{+0.00095}_{-0.00096}$	$0.05299 ^{+0.00077}_{-0.00076}$	Sect. 3.2
$b = (a/R_*) \cos i$	$0.154 ^{+0.107}_{-0.099}$	$0.203 ^{+0.128}_{-0.134}$	$0.819 ^{+0.012}_{-0.013}$	$0.185 ^{+0.133}_{-0.122}$	Sect. 3.2
i	$88.63 ^{+0.89}_{-0.96}$	$88.65 ^{+0.90}_{-0.91}$	$88.21 ^{+0.07}_{-0.08}$	$88.85 ^{+0.76}_{-0.88}$	Sect. 3.2
e	$0.025 ^{+0.023}_{-0.016}$	$0.298 ^{+0.008}_{-0.008}$	$0.272 ^{+0.014}_{-0.014}$	$0.009 ^{+0.003}_{-0.002}$	Sect. 3.2
M_b ($M_{\rm Jup}$)	$3.35 ^{+0.18}_{-0.18}$	$66.98 ^{+2.96}_{-2.95}$	$65.85 ^{+2.75}_{-2.72}$	$67.62 ^{+3.45}_{-3.45}$	Sect. 3.2
R_b ($R_{\rm Jup}$)	$1.30 ^{+0.05}_{-0.05}$	$1.11 ^{+0.05}_{-0.05}$	$1.08 ^{+0.04}_{-0.04}$	$0.95 ^{+0.09}_{-0.09}$	Sect. 3.2
ρ_b (g cm^{-3})	$1.89 ^{+0.23}_{-0.22}$	$61.16 ^{+9.34}_{-9.33}$	$66.06 ^{+8.10}_{-8.09}$	$97.53 ^{+29.35}_{-29.36}$	Sect. 3.2
a (AU)	$0.0561 ^{+0.0024}_{-0.0025}$	$0.1090 ^{+0.0058}_{-0.0064}$	$0.1457 ^{+0.0066}_{-0.0066}$	$0.0788 ^{+0.0079}_{-0.0081}$	Sect. 3.2
$T_{\rm eq}$ (K)	$1728 ^{+27}_{-27}$	$2047 ^{+45}_{-45}$	$982 ^{+17}_{-17}$	$1419 ^{+26}_{-26}$	This work$^{(\alpha)}$
$\langle F \rangle$ (10^8 erg s^{-1} cm^{-2})	$7.24 ^{+1.25}_{-1.26}$	$1.92 ^{+0.35}_{-0.36}$	$1.07 ^{+0.19}_{-0.19}$	$3.67 ^{+0.92}_{-0.93}$	This work$^{(b)}$

Notes. $^{(\alpha)}$ The equilibrium temperature is calculated using $T_{\rm eq} = T_{\rm eff}(1\text{-A})^{1/4} \sqrt{\frac{R_*}{2a}}$, assuming an albedo $A = 0$. $^{(b)}$ The incident flux is calculated using $\langle F \rangle = \frac{L_*}{4\pi a^2}$. $^{(*)}$ refers to the age of TOI-1107 that was constrained in Sect. 4.3.

References. TICv8 (Stassun et al. 2019), 2MASS (Skrutskie et al. 2006), *Gaia* Data Release 2 (Gaia Collaboration 2018), Tycho-2 (Høg et al. 2000).
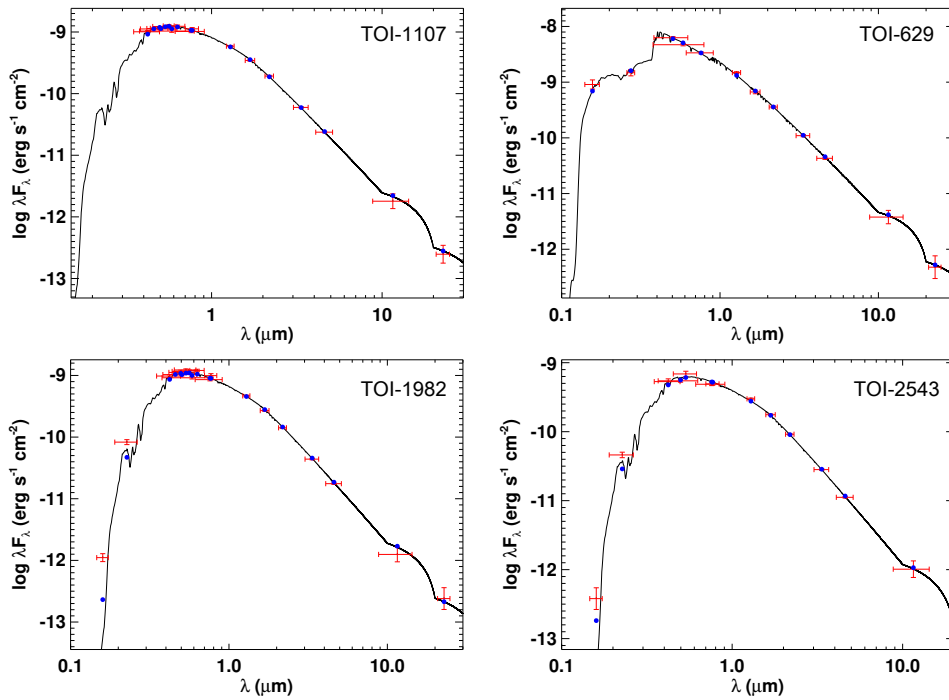
Fig. 5. Spectral energy distributions (SEDs) for the four targets studied in this paper. The red symbols represent the observed photometric measurements, where the horizontal bars represent the effective width of the bandpass, and the blue symbols represent the model fluxes from the best-fit Kurucz stellar atmosphere model (black).

line-of-sight value from the dust maps of Schlegel et al. (1998). In the following paragraphs, we summarize the resulting fit parameters for each system in turn.

TOI-1107: The resulting fit (Fig. 5, top left) has small reduced χ^2 of 1.2. The best fit extinction is $A_V = 0.20 \pm 0.05$ and the bolometric flux at Earth is $F_{bol} = 1.88 \pm 0.02 \times 10^{-9}$ erg s^{-1} cm^{-2}. This gives the stellar radius as $R_* = 1.81 \pm 0.06\ R_\odot$, and the stellar mass from the empirical relations of Torres et al. (2010) is $M_* = 1.35 \pm 0.08\ M_\odot$, consistent with that obtained from $\log g$ and R_* of $M_* = 1.31 \pm 0.18\ M_\odot$. In Sect. 4.3, we provide an estimate of the stellar age using the above stellar radius R_*, the rotation period found in the light curves and the empirical activity-age relations of Mamajek & Hillenbrand (2008).

TOI-629: The resulting fit (Fig. 5, top right) has small reduced χ^2 of 1.2. The best fit extinction is $A_V = 0.37 \pm 0.05$. Integrating the (unreddened) model SED gives the bolometric flux at Earth of $F_{bol} = 10.61 \pm 0.04 \times 10^{-9}$ erg s^{-1} cm^{-2}. Taking the F_{bol} and T_{eff} together with the *Gaia* eDR3 parallax (with no adjustment for systematic offset; see Stassun & Torres 2021), gives the stellar radius as $R_* = 2.37 \pm 0.11\ R_\odot$. Finally, estimating the stellar mass from the empirical relations of Torres et al. (2010) gives $M_* = 2.16 \pm 0.13\ M_\odot$, which is roughly consistent with that obtained empirically via the spectroscopic $\log g$ together with R_*, giving $M_* = 3.25 \pm 0.72\ M_\odot$. In addition, R_* together with the spectroscopic $v \sin i_*$ gives an estimate of the projected rotation period, $P_{rot}/ \sin i_* = 1.77 \pm 0.10$ days. We can integrate the SED at $\lambda < 912$ Å to obtain an estimate of the XUV irradiation from the star at a distance of 1 AU, $F_{XUV,1AU} = 1.2 \pm 0.4$ erg s^{-1} cm^{-2}, though we adopt a factor of 10 systematic error on this flux due to uncertainties in the model atmospheres in the UV (see, e.g., Gaudi et al. 2017, for the example case of KELT-9). Finally, the system appears to be

a kinematic member of the Theia 838 "stellar string". The *Gaia* distance and proper motions (in both right ascension and declination) for this star are consistent with the distributions in distance and proper motion of other stellar members of that association, as determined by Kounkel et al. (2020), giving an estimated age of $\tau_* = 0.32 \pm 0.13$ Gyr.

TOI-1982: The resulting fit (Fig. 5, bottom left) has small reduced χ^2 of 1.5, excluding the GALEX data which suggests chromospheric activity. The best fit extinction is $A_V = 0.01 \pm 0.01$, and the bolometric flux at Earth is $F_{bol} = 1.40 \pm 0.02 \times 10^{-9}$ erg s^{-1} cm^{-2}. This gives the stellar radius as $R_* = 1.51 \pm 0.05\ R_\odot$, and the stellar mass from the empirical relations of Torres et al. (2010) is $M_* = 1.41 \pm 0.08\ M_\odot$, which is somewhat inconsistent with that obtained from $\log g$ and R_* of $M_* = 0.71 \pm 0.10\ M_\odot$, suggesting the spectroscopic $\log g$ in this case is underestimated. We can use the GALEX excess to estimate the chromospheric activity via the empirical relations of Findeisen et al. (2011), giving $\log R'_{HK} = -4.83 \pm 0.10$, which from the empirical activity-age relations of Mamajek & Hillenbrand (2008) gives the system age to be $\tau_* = 3.6 \pm 1.5$ Gyr.

TOI-2543: The resulting fit (Fig. 5, bottom right) has small reduced χ^2 of 0.8, excluding the GALEX photometry which suggests chromospheric activity. The best fit extinction is $A_V = 0.02 \pm 0.02$, and the bolometric flux at Earth is $F_{bol} = 0.77 \pm 0.02 \times 10^{-10}$ erg s^{-1} cm^{-2}. This gives the stellar radius as $R_* = 1.86 \pm 0.15\ R_\odot$, and the stellar mass from the empirical relations of Torres et al. (2010) is $M_* = 1.29 \pm 0.08\ M_\odot$. In addition, R_* together with the spectroscopic $v \sin i_*$ gives an estimate of the projected rotation period, $P_{rot}/ \sin i_* = 8.73 \pm 0.82$ days. Finally, as with TOI-1982 we can estimate the chromospheric activity from the GALEX excess, which gives $\log R'_{HK} = -4.95 \pm 0.05$, yielding an estimated age of $\tau_* = 5.6 \pm 0.9$ Gyr.

All the stellar parameters are listed in Table 2. The stellar mass that we present in the table and use for our analysis is the one estimated from the empirical relations of Torres et al. (2010). The stellar luminosity is calculated using the stellar radius and mass from the table.

3.2. Joint transit and RV analysis

We retrieved the companion parameters of the four systems using a joint photometric and radial-velocity modeling with `juliet` (Espinoza et al. 2019). `juliet` is a publicly available tool that allows to fit both transit models (via `batman` package, Kreidberg 2015) and RVs (via `radvel` package, Fulton et al. 2018) simultaneously and model the noise using Gaussian processes (GPs) (via `celerite` package, Foreman-Mackey et al. 2017). The code uses nested sampling algorithms in order to explore the parameter space with `dynesty` (Speagle 2020) and performs a proper model comparison via Bayesian evidences (lnZ) with `MultiNest` (Feroz et al. 2009) using the `PyMultiNest` (Buchner et al. 2014) Python software package. For the transit model, `juliet` performs an efficient parametrization by fitting for the parameters r_1 and r_2 to ensure uniform exploration of the p (planet-to-star ratio) and b (impact parameter) space. Also, `juliet` fits for the stellar density ρ_* that is combined with the orbital period to provide the scaled semi-major axis (a/R_*).

For our joint analyses we use the TESS light curves, the ground based photometry and the follow-up RV measurements from CORALIE, CHIRON, TRES, FEROS, and MINERVA-Australis. As first step we isolate each TESS transit by applying a cut of 1.5 days before and after each transit midpoint. For our analysis we use the stellar density and its uncertainty derived from our SED fit as a Gaussian prior. The quadratic stellar limb-darkening coefficients and their uncertainties are derived using the LDCU[3] code, a modified version of the python routine implemented by Espinoza & Jordán (2015), for each photometric filter used. LDCU computes the limb-darkening coefficients and their corresponding uncertainties using a set of stellar intensity profiles accounting for the uncertainties on the stellar parameters. For all TESS data the determined limb-darkening coefficients are used as Gaussian priors in our global analysis. The precision of the ground based photometry does not allow us to fit the limb darkening parameters and therefore we keep them fixed. A white-noise jitter term is added in quadrature to the error bars of both photometry and RV data to account for underestimated uncertainties and additional noise that was not captured by our modeling. The jitter terms are first fit using large log-uniform priors. Considering that they are neither significantly different than zero, we decided to fix them to zero. Since there are no significant contamination sources nearby TOI-629, TOI-1982, and TOI-2543 we fix the dilution factor of both TESS and ground photometry to one. For TOI-1107, as we mentioned in Sect. 2.2.1, the contamination from its nearby star (1%) is much smaller than the transit depth uncertainty (5%) therefore the affect is negligible and the dilution factor is fixed to one as well.

We model our TESS data using a Gaussian process (GP) fit independently to the 2-min and 30-min cadence data. To do this, we use a celerite (approximate) Matérn-3/2 kernel (Foreman-Mackey et al. 2017) with hyperparameters amplitude (σ_{GP}) and timescale (ρ_{GP}). The low level of correlated noise in TOI-2543 2-min cadence light curves does not necessitate further detrending. The ground-based photometric data are affected

---

[3] `https://github.com/delinea/LDCU`
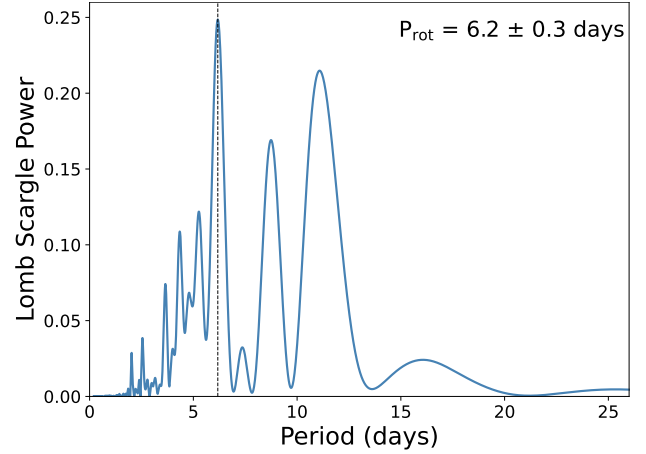
Fig. 6. Lomb-Scargle periodogram from the TESS light SAP-flux Sector 38 and 39 light curves of TOI-1107. The periodogram indicates a peak frequency at 6.2 ± 0.3 days which is in agreement with the rotational period obtained from the CORALIE calibration.

by correlated noise that originates from atmospheric, instrumental or stellar effects. To account for it we use a combination of polynomials in different variables (time, airmass, FWHM, and sky background). To understand the origin of the systematic and find a good combination of polynomials to model each light curve we use the minimization of the Bayesian Information and selected models with the smallest Bayesian information criterion (BIC) and the smallest number of free parameters (less complex model).

For our joint analysis we first fit our radial velocity data with simple Keplerian models on DACE[1] in order to determine mean values for the radial velocity semi-amplitude (K) and the systemic radial velocity (μ). Afterward, we fit wide uniform priors centered on the predicted K and of μ of each companion. The results of the global MCMC analysis of TOI-1107, TOI-629, TOI-1982, and TOI-2543 can be found in Tables B.1 and B.2.

Barnes (2009) demonstrated how the gravity darkening induced by rapid stellar rotation can distort the light curves of any transiting companions, and how this can be used to study the orbital alignment. As our host star analysis reveals that TOI-629 has a $v \sin i_*$ of 56.93 ± 3.61, we test the effect of fitting for a gravity darkening signature in the light curve following the strategy of Hooton et al. (2022). Although a comparison between this fit and `juliet` fit showed no clear evidence for these distortions, a measurement of the orbital alignment from the transit light curve may be possible in the future when more data have been acquired.

4. Discussion

4.1. TOI-1107b: A massive planet transiting a F-type star

TOI-1107b is a massive hot Jupiter with an estimated mass of 3.35 ± 0.18 M_{Jup} and a radius of 1.30 ± 0.05 R_{Jup} that transits a F6V star with a period of $4.0782387^{+0.0000024}_{-0.0000025}$ days. To date, only 17 confirmed planets more massive than 3 M_{Jup} with well-constrained densities ($\sigma_M/M \leq 25\%$ and $\sigma_R/R \leq 8\%$) orbiting stars with $T_{eff} > 6200$ K have been identified (PlanetS catalog of Otegi et al. (2020), accessible on the Data & Analysis Center for Exoplanet DACE[1]).

Massive planets are scientifically interesting since they can provide insight into the planet formation processes at the

Fig. 7. Eccentricity-companion mass distribution of known massive planets (from the updated exoplanet catalog of Otegi et al. 2020) and transiting brown dwarfs (Table 3). The different colors indicate the orbital period. The massive planet (TOI-1107b) and three brown dwarfs (TOI-629b, TOI-1982b, and TOI-2543b) presented in this work are displayed with yellow edge color.

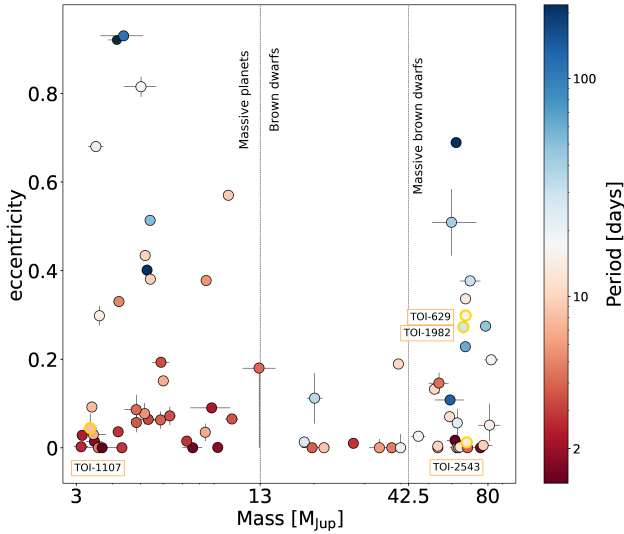transition between giant massive planets and brown dwarfs. Santos et al. (2017) studied the statistical properties of giant planets, together with those of their host stars in a search for clues about the process of planet formation and evolution. The results suggested that there are two distinct giant planet populations with masses above and below $\sim 4\,M_{\rm Jup}$. More specifically, they found that lower-mass planets may form by the core-accretion process and orbit metal-rich stars, while more massive giant planets may form via disk instability and their hosts have lower average metallicity values. This theory was corroborated by Schlaufman (2018) who found that planets with masses $\lesssim 4\,M_{\rm Jup}$ orbit preferentially more metal-rich stars, unlike planets with masses $\gtrsim 10\,M_{\rm Jup}$ that do not share this property. With a metallicity of [Fe/H] $= -0.10 \pm 0.09$ the TOI-1107 system is not consistent with the theory presented in the above studies.

4.2. Massive planet and BD eccentricity distribution

Figure 7 shows the eccentricity distribution for massive planets and transiting brown dwarfs. The color of each point denotes the orbital period. The first vertical line ($13\,M_{\rm Jup}$) represents the transition between massive planets and low-mass brown dwarfs and the second ($42.5\,M_{\rm Jup}$) the transition between low-mass and high-mass brown dwarfs.

TOI-629b is a $67.0 \pm 3.0\,M_{\rm Jup}$ brown dwarf with a radius of $1.11 \pm 0.05\,R_{\rm Jup}$ that transits a A2V star with a period of $8.717993^{+0.000012}_{-0.000013}$ days. TOI-1982b is a brown dwarf with a mass of $65.8 \pm 2.7\,M_{\rm Jup}$ and a radius of $1.08 \pm 0.04\,R_{\rm Jup}$ transiting a F7V star with a period of $17.172446^{+0.000043}_{-0.000044}$ days. TOI-2543b is a $67.6 \pm 3.4\,M_{\rm Jup}$ massive brown dwarf with a radius of $0.95 \pm 0.09\,R_{\rm Jup}$ that transits a F9V star with a period of 7.542776 ± 0.000031 days. The diagram places TOI-629 and TOI-1982 among the most eccentric systems with eccentricities of 0.298 ± 0.008 and 0.272 ± 0.014, respectively. The detections of TOI-629b and TOI-1982b are consistent with the Ma & Ge (2014) observations regarding the different eccentricity distribution of brown dwarfs with masses greater and lower than

$42.5\,M_{\rm Jup}$. More specifically, there is strong evidence that brown dwarfs less massive than $42.5\,M_{\rm Jup}$ tend to have lower eccentricities while brown dwarfs with masses above this threshold have higher and more diverse eccentricities. This could be explained by the different formation mechanisms with the less massive being formed via disk gravitational instability (Boss 1997) and the more massive through molecular cloud fragmentation (Hennebelle & Chabrier 2008), similar to the formation of stellar binaries. Since the eccentricity distribution of these targets is consistent with that of binary stars, we see that there are no eccentric brown dwarfs at short periods ($\lesssim 10$ days), which can be explained by the tidal circularization effect (Adams & Laughlin 2006). Massive planets show more diversity in their eccentricities compared to the brown dwarf population. TOI-1107b has a low, typical eccentricity which is compatible with planets with similar masses.

4.3. Stellar rotation

From the full width at half maximum (FWHM) of the CORALIE cross-correlation function (CCF) we manage to estimate the projected rotational velocities of the four targets. With their color index B-V and stellar radius R_* We estimate an upper limit on the stellar rotation period ($P_{\rm rot} \leq 2\pi R_*/v \sin i_*$) and compare it with the orbital period in order to examine possible spin–orbit synchronization.

For TOI-1107, we estimate a projected rotational velocity of $v \sin i_* = 12.31 \pm 0.79$ km s^{-1} using the CORALIE spectra. Since the PDCSAP light curve for TOI-1107 shows stellar variability we use a Lomb-Scargle periodogram and estimate a rotation period of $P_{\rm rot} = 6.2 \pm 0.3$ days (Fig. 6). With the derived stellar radius R_* and projected rotational velocity we estimate the upper limit of TOI-1107 rotation period $P_{\rm rot}/\sin i_* = 7.44 \pm 0.65$ days which is in agreement with the 6.2 days modulation found in the light curves. Compared to its orbital period ($P_{\rm orb} = 4.0782387^{+0.0000024}_{-0.0000025}$ days), TOI-1107b does not provide any conclusive evidence of spin–orbit synchronization. Using the rotation period from the periodogram, the stellar radius R_* and gyrochronology relations of Mamajek & Hillenbrand (2008) we find an age estimate of 2.6 ± 0.2 Gyr which indicates that TOI-1107 is a relatively old F-type star. Our global analysis gives an eccentricity $e = 0.025^{+0.023}_{-0.016}$, which we find not significant using the Lucy & Sweeney (1971) test and compatible with a circular orbit. Using Equation (3) from Adams & Laughlin (2006) we find that TOI-1107b has a circularization timescale of ~ 0.2 Gyr for a tidal quality factor $Q_{\rm p} = 10^5$ and ~ 2 Gyr for a tidal quality factor $Q_{\rm p} = 10^6$. That suggests that the massive planet orbit might have undergone tidal circularization but not spin–orbit synchronization. TOI-629 is an A-type, rapidly rotating star ($P_{\rm rot}/\sin i_* = 1.77 \pm 0.10$ days). Given its young age (0.32 ± 0.13 Gyr) and its orbital period $P_{\rm orb} = 8.717993^{+0.000012}_{-0.000013}$ days we find no evidence of spin–orbit synchronization. TOI-1982 is a relatively old (3.6 ± 1.5 Gyr) and fast rotating star ($P_{\rm rot}/\sin i_* = 2.03 \pm 0.15$). Given its long orbital period of $17.172446^{+0.000043}_{-0.000044}$ days, TOI-1982b is unlikely to have reached spin–orbit synchronization. TOI-2543 is the oldest of our targets, with an estimated age of 5.6 ± 0.9 Gyr and a companion on a nearly circular $e = 0.009^{+0.003}_{-0.002}$ orbit. From the SED analysis we estimate a projected rotation period of $P_{\rm rot}/\sin i_* = 8.73 \pm 0.82$ days. Taking into account that it is approximately one day larger than the orbital period (7.542776 ± 0.000031 days), we suspect that TOI-2543b can be in a state of spin–orbit synchronization. Assuming a lower bound on the tidal quality factor $Q_{\rm p} = 10^{4.5}$ (Beatty et al. 2018), the circularization
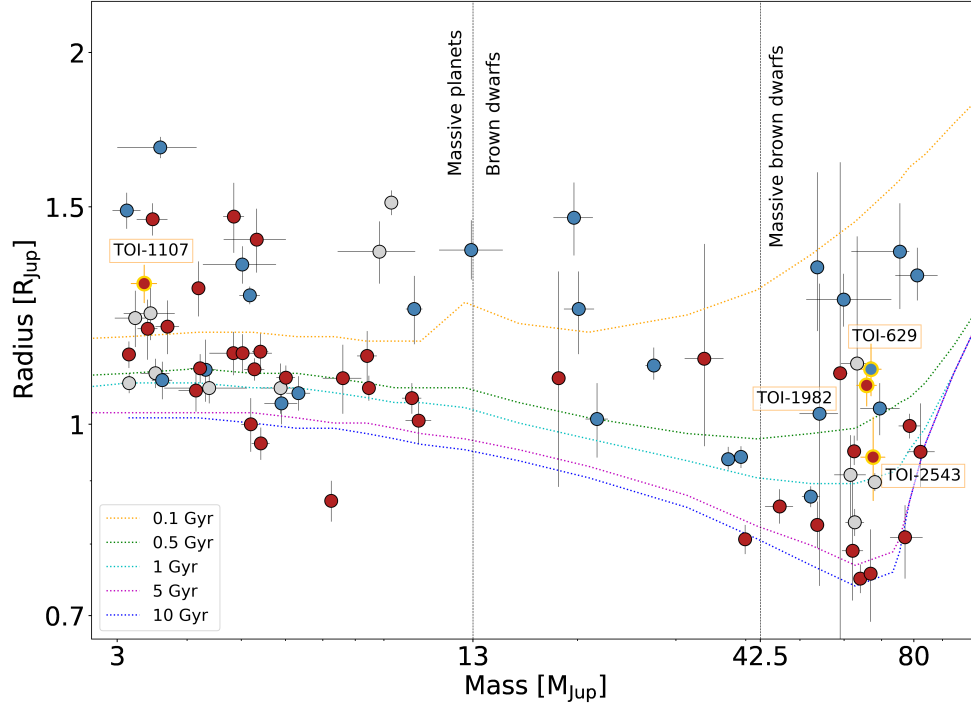
Fig. 8. Radius–mass diagram of all massive planets ($M_p > 3\ M_{Jup}$, from the updated exoplanet catalog of Otegi et al. 2020) and transiting brown dwarfs (Table 3). The colored lines indicate the isochrone models (Baraffe et al. 2003, 2015). The red color of the points denotes old stars (≥ 2 Gyr), the blue young stars (< 2 Gyr) and the gray not reported age. The brown dwarf RIK 72b (David et al. 2019) is not plotted because of its large radius ($3.1\ R_{Jup}$). The massive planet and three brown dwarfs presented in this work are displayed with yellow edge color.

timescale for TOI-2543b corresponds to ~60 Gyr indicating that we would not expect the system to have been tidally circularized yet.

4.4. Mass–radius relation

We place TOI-1107b in the mass–radius diagram of transiting massive planets ($>3\ M_{Jup}$) and brown dwarfs (Fig. 8). We color the symbols based on the stellar age where the blue color indicates young stars (<2 Gyr), the red color indicates old stars (≥ 2 Gyr) and the gray color indicates stars with no reported age. Also, we plot the theoretical evolutionary models from Baraffe et al. (2003, 2015) for ages of 0.1, 0.5, 1, 5, and 10 Gyr with different colors. As described in Sect. 4.3 We derived an age of 2.6 ± 0.2 Gyr for TOI-1107. Compared to the standard evolutionary tracks (Baraffe et al. 2003, 2015), TOI-1107b with a radius of $1.30 \pm 0.05\ R_{Jup}$, appears to be inflated by ~20%. Accordingly, we determine the luminosity with the derived stellar radius and effective temperature of our analysis (Table 2). Using the semi-major axis of the orbit (Table B.2) we calculate an incident flux of $\langle F \rangle = (2.02^{+0.16}_{-0.26}) \times 10^6$ W m^{-2} (1480^{+115}_{-191} S$_\oplus$), which is approximately 10 times larger than the empirical inflation boundary of $\langle F \rangle = 2 \times 10^5$ W m^{-2} (Miller & Fortney 2011; Demory & Seager 2011). Thus, we expect that the radius of this planet is larger than theoretically predicted. Sestovic et al. (2018) performed a detailed analysis of the relationship between the planetary radius, mass, and stellar irradiation by studying the population of transiting gas giants with four different mass regimes. With a mass of $3.35\ M_{Jup}$, TOI-1107b lies above the highest mass boundary ($M_p > 2.5\ M_{Jup}$) and the predicted excess radius is $\Delta R = 0.221^{+0.007}_{-0.011}\ R_{Jup}$ (Equation (11), Sestovic et al. 2018). Given a mass of ~$3.35\ M_{Jup}$, an age of ~2.6 Gyr and following the theoretical models of planet evolution (Baraffe et al.

2003, 2015) the predicted radius of TOI-1107b ranges from 1 to 1.1 R_{Jup}. With an observed radius of $1.30 \pm 0.05\ R_{Jup}$, TOI-1107b has an inflated radius that is in agreement with the empirical relation proposed by Sestovic et al. (2018). The radius excess of hot Jupiters can be explained by different mechanisms that arise from the strong stellar irradiation such as vertical advection of the potential temperature (Tremblin et al. 2017), thermal tidal effects (Arras & Socrates 2010), and Ohmic dissipation through magnetohydrodynamic effects (Batygin & Stevenson 2010).

We place the three brown dwarfs in the mass–radius diagram and compare their estimated age from the spectral analysis with the theoretical isochrones. Both TOI-629b and TOI-2543b have masses and radii that are consistent with the theoretical models (Baraffe et al. 2003, 2015) taking into account their radius uncertainties. With an age of 3.6 ± 1.5 Gyr and a radius of $1.08 \pm 0.04\ R_{Jup}$, TOI-1982b appears to be significantly inflated with respect to the theoretical radius of $0.82 \pm 0.04\ R_{Jup}$ (Baraffe et al. 2003, 2015). Such effect has been detected in massive, transiting brown dwarfs before, for example in CoRoT-15b (Bouchy et al. 2011b) and NGTS-19b (Acton et al. 2021).

4.5. Transiting massive planet and BD population

Figure 9 shows the mass distribution over the stellar effective temperature for all known transiting massive planets and brown dwarfs, including the four new companions presented in this work. The symbol size is inversely proportional to the brown dwarf's period. Based on the lists compiled by Carmichael et al. (2021) and Grieves et al. (2021) and including the discoveries of TOI-629b, TOI-1982b, and TOI-2543b, the total number of transiting brown dwarfs is 36 (Table 3). TESS has strongly contributed to the number of these relatively rare objects with 13 detections (red symbols) over the first 3 yr of its operation.
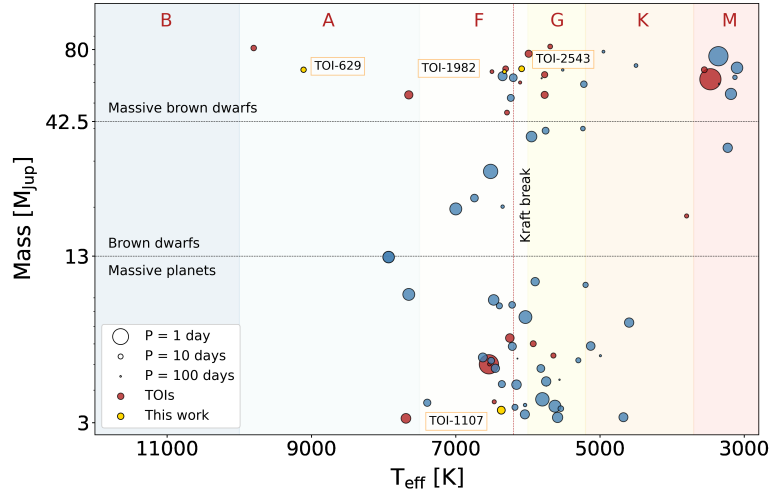
Fig. 9. Companion mass over stellar effective temperature T_{eff} diagram for massive planets ($M_P > 3 \, M_{Jup}$, from the updated exoplanet catalog of Otegi et al. 2020) and transiting brown dwarfs (Table 3) shown in blue. The four new companions are shown in yellow. The red circles display confirmed companions detected by TESS. The size scales inversely with the period of the companion. The red, vertical line corresponds to the Kraft break (6200 K) while the horizontal lines correspond to the approximate boundaries of the brown dwarf regime (13 M_{Jup}) and the transition to high-mass brown dwarfs (42.5 M_{Jup}).

The current brown dwarf population is sparse and distributes over a large stellar effective temperature range with a significant low occurrence of lighter brown dwarfs (13–42.5 M_{Jup}) compared to more massive brown dwarfs (42.5–80 M_{Jup}). As discussed in Sect. 4.2, this suggests two different formation mechanisms between the two populations. The sample is not large enough for meaningful comparison, however we see that 20% of the population is hosted by M-dwarf stars, ~8% by K-type stars, ~29% by G-type stars and ~31% by F-type. To date there are only four detected brown dwarfs transiting A stars: HATS-70b (Zhou et al. 2019), TOI-503b (Šubjak et al. 2020), TOI-587b (Grieves et al. 2021), and TOI-629b (this work). TOI-629 with T_{eff} = 9100 ± 200 K is the second hottest star to host a brown dwarf after TOI-587b, a brown dwarf or very low-mass star transiting an A-type star with T_{eff} = 9800 ± 200 K. This paucity could possibly be an observational bias in the spectroscopic follow-up strategy toward such hot candidates. No transiting brown dwarfs have been detected orbiting B or hotter type stars. The planet and brown dwarf occurrence rate around OB stars is unknown due to observational difficulties. *Gaia* (Gaia Collaboration 2018) will allow the coverage of this stellar population by revealing astrometric signals of massive companions at intermediate orbital periods. As shown in Fig. 9 and mentioned by Udry et al. (2003), Bouchy et al. (2011a) and Grieves et al. (2021), there is a significant lack of short period ($P < 10$ days), massive companions orbiting K- and G-type stars. This could be possibly explained by the magnetic braking of G- and K-type stars that is is expected to spin down the star and drive ongoing decay of the companion (Barker & Ogilvie 2009). This effect will result in inward migration and eventually engulfment of the companion by its host star. In contrast, F-type stars undergo less magnetic braking, avoid losing their angular momentum and the decay timescale is expected to be longer, resulting in larger number of massive companions around these stars.

4.6. Four EBLM systems

As a by-product of this RV follow-up, we identified four low mass, single-lined spectral eclipsing binaries observed with CORALIE spectrograph. All targets were initially detected photometrically by TESS over the first 3 yr of its operation. The stellar parameters of the primary star were obtained from `SpecMatch-Emp` on the stacked CORALIE spectra as described in Sect. 3.1.1. Our RV measurements reveal that these four F-type primary stars host companions with masses ranging from ~156–332 M_{Jup}. The stellar properties of the primary and secondary stars are listed in Table C.1 and their phase-folded radial velocities with the best-fit Keplerian model in Fig. C.1.

TOI-288 (TIC 47316976) was observed in TESS Sector 2 and 28 and two shallow transits with a depth of ~0.17% Were identified with an interval of 711.74 days. The RV measurements with CORALIE revealed a 332.4 ± 41.8 M_{Jup} low-mass companion with orbital period P_{orb} = 79.08 days and time of conjunction consistent with secondary eclipse. TESS did not observe the main eclipse of the long period eccentric binary system but only the secondary eclipse. As described by Santerne et al. (2013), long-period candidates with eccentric orbit that present a secondary-only eclipse, are more likely to be false positives. Also, 26 out of 37 of our candidates with a transit depth larger than ~1.5% reveal to be eclipse binaries which is in agreement with the follow-up of Kepler giant planet candidates described by Santerne et al. (2016). Low-mass stars are ideal for Earth-sized planet detection and characterization. However, this sample is limited when compared to more massive stars because they are intrinsically dimmer. These four targets add to this population and can be used for future stellar characterization and enable an empirical mass–radius exploration.

5. Conclusion

In the context of the search for exoplanets and brown dwarfs around early-type main-sequence stars, we present the discovery and characterization of three high-mass brown dwarfs, TOI-629b, TOI-1982b, TOI-2543b, and one massive planet, TOI-1107b, identified by the TESS mission. Our analysis is based on both 2-min and QLP TESS data from several sectors in the first and third years of operations. The detections were confirmed

Table 3. List of published transiting brown dwarfs as of December 2021.

Name	M_2 (M_{Jup})	R_2 (R_{Jup})	P (days)	D (mmag)	ecc	M_1 ($M_\odot$)	R_1 ($R_\odot$)	T_{eff} (K)	[Fe/H]	Ref.
HATS-70b	$12.9^{+1.8}_{-1.6}$	$1.38^{+0.08}_{-0.07}$	1.89	5.928	<0.18	1.78 ± 0.12	$1.88^{+0.06}_{-0.07}$	7930^{+630}_{-820}	$0.04^{+0.10}_{-0.11}$	(1)
TOI-1278b	18.5 ± 0.5	$1.09^{+0.24}_{-0.20}$	14.48	40.041	0.013 ± 0.004	0.54 ± 0.02	0.57 ± 0.01	3799 ± 42	-0.01 ± 0.28	(2)
GPX-1b	19.7 ± 1.6	1.47 ± 0.10	1.74	9.723	0.000 ± 0.000	1.68 ± 0.10	1.56 ± 0.10	7000 ± 200	0.35 ± 0.10	(3)
Kepler-39b	$20.1^{+1.3}_{-1.2}$	$1.24^{+0.09}_{-0.10}$	21.09	8.590	0.112 ± 0.057	$1.29^{+0.06}_{-0.07}$	1.40 ± 0.10	6350 ± 100	0.10 ± 0.14	(4)
CoRoT-3b	21.7 ± 1.0	1.01 ± 0.07	4.26	4.590	0 (fixed)	1.37 ± 0.09	1.56 ± 0.09	6740 ± 140	-0.02 ± 0.06	(5)
KELT-1b	27.4 ± 0.9	$1.12^{+0.04}_{-0.03}$	1.22	6.302	$0.010^{+0.010}_{-0.007}$	1.33 ± 0.06	1.47 ± 0.04	6516 ± 49	0.05 ± 0.08	(6)
NLTT 41135b	$33.7^{+2.8}_{-2.6}$	$1.13^{+0.27}_{-0.17}$	2.89	317.042	<0.02	$0.19^{+0.03}_{-0.02}$	$0.21^{+0.02}_{-0.01}$	3230 ± 130	-0.25 ± 0.25	(7)
WASP-128b	37.2 ± 0.8	0.94 ± 0.02	2.21	7.244	<0.007	1.16 ± 0.04	1.15 ± 0.02	5950 ± 50	0.01 ± 0.12	(8)
CWW 89Ab	$39.2^{+0.9}_{-1.1}$	0.94 ± 0.02	5.29	9.157	0.189 ± 0.002	1.10 ± 0.04	1.03 ± 0.02	5755 ± 49	0.20 ± 0.09	(9) (10)
KOI-205b	39.9 ± 1.0	0.81 ± 0.02	11.72	10.082	<0.031	0.93 ± 0.03	0.84 ± 0.02	5237 ± 60	0.14 ± 0.12	(11)
TOI-1406b	$46.0^{+2.6}_{-2.7}$	0.86 ± 0.03	10.57	4.423	$0.026^{+0.013}_{-0.010}$	$1.18^{+0.08}_{-0.09}$	1.35 ± 0.03	6290 ± 100	-0.08 ± 0.09	(12)
EPIC 212036875b	52.3 ± 1.9	0.87 ± 0.02	5.17	3.727	0.132 ± 0.004	$1.29^{+0.07}_{-0.06}$	1.50 ± 0.03	6238^{+59}_{-60}	0.01 ± 0.10	(10) (13)
TOI-503b	53.7 ± 1.2	$1.34^{+0.26}_{-0.15}$	3.68	6.803	0 (fixed)	1.80 ± 0.06	$1.70^{+0.05}_{-0.04}$	7650^{+140}_{-160}	$0.30^{+0.08}_{-0.09}$	(14)
TOI-852b	$53.7^{+1.4}_{-1.3}$	0.83 ± 0.04	4.95	2.573	$0.004^{+0.004}_{-0.003}$	$1.32^{+0.05}_{-0.04}$	1.71 ± 0.04	5768^{+84}_{-81}	0.33 ± 0.09	(15)
AD 3116b	54.2 ± 4.3	1.02 ± 0.28	1.98	124.696	0.146 ± 0.024	0.28 ± 0.02	0.29 ± 0.08	3184 ± 29	0.16 ± 0.10	(16)
CoRoT-33b	$59.0^{+1.8}_{-1.7}$	1.10 ± 0.53	14.994	5.82	0.070 ± 0.002	0.86 ± 0.04	$0.94^{+0.14}_{-0.08}$	5225 ± 80	0.44 ± 0.10	(17)
RIK 72b	$59.2^{+6.8}_{-6.7}$	3.10 ± 0.31	97.76	113.94	$0.108^{+0.012}_{-0.006}$	0.44 ± 0.04	0.96 ± 0.10	3349 ± 142	0.00 ± 0.10	(18)
TOI-811b	$59.9^{+13.0}_{-8.6}$	1.26 ± 0.06	25.17	10.812	0.509 ± 0.075	$1.32^{+0.05}_{-0.07}$	$1.27^{+0.06}_{-0.09}$	6107 ± 77	$0.40^{+0.07}_{-0.09}$	(15)
TOI-263b	61.6 ± 4.0	0.91 ± 0.07	0.56	47.264	$0.017^{+0.009}_{-0.010}$	0.44 ± 0.04	0.44 ± 0.03	3471 ± 33	0.00 ± 0.10	(19)
KOI-415b	62.1 ± 2.7	$0.79^{+0.12}_{-0.07}$	166.79	4.374	0.689 ± 0.000	0.94 ± 0.06	$1.25^{+0.15}_{-0.10}$	5810 ± 80	-0.24 ± 0.11	(20)
WASP-30b	62.5 ± 1.2	$0.95^{+0.03}_{-0.02}$	4.16	5.133	0 (fixed)	$1.25^{+0.03}_{-0.04}$	1.39 ± 0.03	6202^{+42}_{-51}	$0.08^{+0.07}_{-0.05}$	(21)
LHS 6343c	62.7 ± 2.4	0.83 ± 0.02	12.71	53.175	0.056 ± 0.032	0.37 ± 0.01	0.38 ± 0.01	3130 ± 20	0.04 ± 0.08	(22)
CoRoT-15b	63.3 ± 4.1	$1.12^{+0.30}_{-0.15}$	3.06	6.444	0 (fixed)	1.32 ± 0.12	$1.46^{+0.31}_{-0.14}$	6350 ± 200	0.10 ± 0.20	(23)
TOI-569b	$64.1^{+1.9}_{-1.4}$	0.75 ± 0.02	6.56	2.812	$0.002^{+0.002}_{-0.001}$	1.21 ± 0.05	1.48 ± 0.03	5768^{+110}_{-92}	$0.29^{+0.09}_{-0.08}$	(12)
TOI-1982b	65.8 ± 2.8	1.08 ± 0.04	17.17	5.801	0.272 ± 0.014	1.41 ± 0.08	1.51 ± 0.05	6325 ± 110	-0.10 ± 0.09	this work
EPIC 201702477b	66.9 ± 1.7	0.76 ± 0.07	40.74	7.729	0.228 ± 0.003	0.87 ± 0.03	0.90 ± 0.06	5517 ± 70	-0.16 ± 0.05	(24)
TOI-629b	67.0 ± 3.0	1.11 ± 0.05	8.72	2.503	0.299 ± 0.008	2.16 ± 0.13	2.37 ± 0.11	9100 ± 200	0.10 ± 0.15	this work
TOI-2119b	67 ± 2	1.11 ± 0.03	7.2	51.869	0.3362 ± 0.0005	0.53 ± 0.02	0.51 ± 0.01	3553 ± 67	0.1 ± 0.1	(25)
TOI-2543b	67.6 ± 3.5	0.95 ± 0.09	7.543	3.064	0.009 ± 0.002	1.29 ± 0.08	1.86 ± 0.15	6060 ± 82	-0.28 ± 0.10	this work
LP261-75b	68.1 ± 2.1	0.90 ± 0.01	1.88	90.071	<0.007	0.30 ± 0.01	0.31 ± 0.00	3100 ± 50	...	(26)
NGTS-19b	$69.5^{+5.7}_{-5.4}$	1.03 ± 0.05	17.84	23.044	0.377 ± 0.006	0.73 ± 0.08	0.71 ± 0.10	4500 ± 110	0.09 ± 0.09	(27)
NGTS-7Ab	$75.5^{+3.0}_{-13.7}$	$1.38^{+0.13}_{-0.14}$	0.68	56.04	0 (fixed)	0.24 ± 0.03	0.61 ± 0.06	3359^{+106}_{-89}	0.00 ± 0.10	(28)
KOI-189b	78.6 ± 3.5	1.00 ± 0.02	30.36	20.257	0.275 ± 0.004	0.76 ± 0.05	0.73 ± 0.02	4952 ± 40	-0.12 ± 0.10	(29)
TOI-148b	$77.1^{+5.8}_{-4.6}$	$0.81^{+0.05}_{-0.06}$	4.87	4.989	$0.005^{+0.006}_{-0.004}$	$0.97^{+0.12}_{-0.09}$	1.20 ± 0.07	5990 ± 140	-0.24 ± 0.25	(30)
TOI-587b	$81.1^{+7.1}_{-7.0}$	$1.32^{+0.07}_{-0.06}$	8.04	4.722	$0.051^{+0.049}_{-0.036}$	2.33 ± 0.12	2.01 ± 0.09	9800 ± 200	$0.08^{+0.11}_{-0.12}$	(30)
TOI-746b	$82.2^{+4.9}_{-4.4}$	$0.95^{+0.09}_{-0.06}$	10.98	10.503	0.199 ± 0.003	$0.94^{+0.09}_{-0.08}$	$0.97^{+0.04}_{-0.03}$	5690 ± 140	-0.02 ± 0.23	(30)

Notes: We do not include the brown dwarf binary system by Stassun et al. (2006), triple system by Triaud et al. (2020), and white dwarf companions.
References. (1) Zhou et al. 2019; (2) Artigau et al. 2021; (3) Benni et al. 2021; (4) Bonomo et al. 2015; (5) Deleuil et al. 2008; (6) Siverd et al. 2012; (7) Irwin et al. 2010; (8) Hodžić et al. 2018; (9) Nowak et al. 2017; (10) Carmichael et al. 2019; (11) Díaz et al. 2013; (12) Carmichael et al. 2020; (13) Persson et al. 2019; (14) Šubjak et al. 2020; (15) Carmichael et al. 2021; (16) Gillen et al. 2017; (17) Csizmadia et al. 2015; (18) David et al. 2019; (19) Palle et al. 2021; (20) Moutou et al. 2013; (21) Triaud et al. 2013; (22) Johnson et al. 2011; (23) Bouchy et al. 2011b; (24) Bayliss et al. 2017; (25) Cañas et al. 2022; (26) Irwin et al. 2018; (27) Acton et al. 2021; (28) Jackman et al. 2019; (29) Díaz et al. 2014; (30) Grieves et al. 2021.

via numerous ground-based photometric observations and RV observations with the CORALIE, CHIRON, TRES, FEROS, and MINERVA-Australis spectrographs. The stellar and companion parameters are summarized in Table 2.

TOI-629 is the second hottest main-sequence star (T_{eff} = 9100 ± 200 K) known to host a brown dwarf (M_b = $66.98^{+2.96}_{-2.95}$ M_{Jup}) and among the most eccentric systems (e = 0.298 ± 0.008). Its high projected stellar rotation velocity required investigation of the stellar rotation-induced gravity darkening effect in the TESS light curves with no evidence of distortion.

TOI-1982b is a massive brown dwarf (M_b = $65.85^{+2.75}_{-2.72}$ M_{Jup}) on an eccentric orbit (e = 0.272 ± 0.014) around an F-type (T_{eff} = 6325 ± 110 K) star. The systems age

determination from the SED analysis relative to theoretical predictions indicates that TOI-1982b is significantly inflated.

TOI-2543 is an F-type star, (T_{eff} = 6060 ± 82 K) that hosts a 67.62 ± 3.45 M_{Jup} massive brown dwarf on a nearly circular orbit (e = $0.009^{+0.003}_{-0.002}$). The SED analysis estimates that its projected rotation period is one day larger that the brown dwarfs orbital period, indicating that TOI-2543b can be in a state of spin–orbit synchronization but the system has not been tidally circularized yet.

TOI-1107b is a 3.35 ± 0.18 M_{Jup} hot Jupiter with an orbital period of 4.08 days, transiting an F-type (T_{eff} = 6311 ± 98 K) star. Based on the host star's rotation period that was identified in its light curve we estimated the age of the system (τ_* = 2.6 ± 0.2 Gyr). When compared to theoretical isochrone models,

TOI-1107b presents an inflated radius due to irradiation from their host star.

The discoveries of TOI-1107b, TOI-629b, TOI-1982b, and TOI-2543b add to the population of exoplanets and brown dwarfs with well-determined radii and masses (i.e., $\sigma_R/R < 10\%$ and $\sigma_M/M < 5\%$), transiting AF-type stars. Finally, we present four binary systems with low-mass eclipsing components (TOI-288b, TOI-446b, TOI-478b, and TOI-764b) transiting F-type stars that were detected with CORALIE. Continuation of photometric and radial velocity surveys around early-type stars will allow further investigation on how stellar mass impacts planet and brown dwarf formation and evolution.

References

Abe, L., Gonçalves, I., Agabi, A., et al. 2013, A&A, 553, A49
Acton, J. S., Goad, M. R., Burleigh, M. R., et al. 2021, MNRAS, 505, 2741
Adams, F. C., & Laughlin, G. 2006, ApJ, 649, 1004
Addison, B., Wright, D. J., Wittenmyer, R. A., et al. 2019, PASP, 131, 115003
Addison, B. C., Knudstrup, E., Wong, I., et al. 2021, AJ, 162, 292
Aller, A., Lillo-Box, J., Jones, D., Miranda, L. F., & Barceló Forteza, S. 2020, A&A, 635, A128
Arras, P., & Socrates, A. 2010, ApJ, 714, 1
Artigau, É., Hébrard, G., Cadieux, C., et al. 2021, AJ, 162, 144
Baraffe, I., Chabrier, G., Barman, T. S., Allard, F., & Hauschildt, P. H. 2003, A&A, 402, 701
Baraffe, I., Homeier, D., Allard, F., & Chabrier, G. 2015, A&A, 577, A42
Baranne, A., Queloz, D., Mayor, M., et al. 1996, A&As, 119, 373
Barker, A. J., & Ogilvie, G. I. 2009, MNRAS, 395, 2268
Barnes, J. W. 2009, ApJ, 705, 683
Batygin, K., & Stevenson, D. J. 2010, ApJ, 714, L238
Bayliss, D., Hojjatpanah, S., Santerne, A., et al. 2017, AJ, 153, 15
Beatty, T. G., Morley, C. V., Curtis, J. L., et al. 2018, AJ, 156, 168
Benni, P., Burdanov, A. Y., Krushinsky, V. V., et al. 2021, MNRAS, 505, 4956
Blanco-Cuaresma, S., Soubiran, C., Heiter, U., & Jofré, P. 2014, A&A, 569, A111
Bonomo, A. S., Sozzetti, A., Santerne, A., et al. 2015, A&A, 575, A85
Borgniet, S., Boisse, I., Lagrange, A. M., et al. 2014, A&A, 561, A65
Borgniet, S., Lagrange, A. M., Meunier, N., & Galland, F. 2017, A&A, 599, A57
Borgniet, S., Lagrange, A. M., Meunier, N., et al. 2019, A&A, 621, A87
Boss, A. P. 1997, Science, 276, 1836
Bouchy, F., & the Sophie Team. 2006, in Tenth Anniversary of 51 Peg-b: Status of and Prospects for Hot Jupiter Studies, eds. L. Arnold, F. Bouchy, & C. Moutou, 319
Bouchy, F., Bonomo, A. S., Santerne, A., et al. 2011a, A&A, 533, A83
Bouchy, F., Deleuil, M., Guillot, T., et al. 2011b, A&A, 525, A68
Brahm, R., Jordán, A., & Espinoza, N. 2017, PASP, 129, 034002
Brown, T. M., Baliber, N., Bianco, F. B., et al. 2013, PASP, 125, 1031
Buchhave, L. A., Latham, D. W., Johansen, A., et al. 2012, Nature, 486, 375
Buchner, J., Georgakakis, A., Nandra, K., et al. 2014, A&A, 564, A125
Cañas, C. I., Mahadevan, S., Bender, C. F., et al. 2022, AJ, 163, 89
Carmichael, T. W., Latham, D. W., & Vand erburg, A. M. 2019, AJ, 158, 38
Carmichael, T. W., Quinn, S. N., Mustill, A. J., et al. 2020, AJ, 160, 53
Carmichael, T. W., Quinn, S. N., Zhou, G., et al. 2021, AJ, 161, 97
Casewell, S. L., Lawrie, K. A., Maxted, P. F. L., et al. 2015, MNRAS, 447, 3218
Castelli, F., & Kurucz, R. L. 2004, A&A, 419, 725
Chelli, A. 2000, A&A, 358, L59
Collier Cameron, A., Guenther, E., Smalley, B., et al. 2010, MNRAS, 407, 507
Collins, K. A., Kielkopf, J. F., Stassun, K. G., & Hessman, F. V. 2017, AJ, 153, 77
Collins, K. A., Quinn, S. N., Latham, D. W., et al. 2018, in American Astronomical Society Meeting Abstracts #231, 439.08
Csizmadia, S., Hatzes, A., Gandolfi, D., et al. 2015, A&A, 584, A13
David, T. J., Hillenbrand, L. A., Gillen, E., et al. 2019, ApJ, 872, 161
Deleuil, M., Deeg, H. J., Alonso, R., et al. 2008, A&A, 491, 889
Demory, B.-O., & Seager, S. 2011, ApJS, 197, 12
Desort, M., Lagrange, A. M., Galland, F., et al. 2008, A&A, 491, 883
Desort, M., Lagrange, A. M., Galland, F., et al. 2009, A&A, 506, 1469
Díaz, R. F., Damiani, C., Deleuil, M., et al. 2013, A&A, 551, A9
Díaz, R. F., Montagnier, G., Leconte, J., et al. 2014, A&A, 572, A109
Dong, J., Huang, C. X., Zhou, G., et al. 2021, ApJ, 920, L16
Dorval, P., Talens, G. J. J., Otten, G. P. P. L., et al. 2020, A&A, 635, A60
Doyle, A. P., Davies, G. R., Smalley, B., Chaplin, W. J., & Elsworth, Y. 2014, MNRAS, 444, 3592
Espinoza, N., & Jordán, A. 2015, MNRAS, 450, 1879
Espinoza, N., Kossakowski, D., & Brahm, R. 2019, MNRAS, 490, 2262
Fabrycky, D., & Tremaine, S. 2007, ApJ, 669, 1298
Feroz, F., Hobson, M. P., & Bridges, M. 2009, MNRAS, 398, 1601
Findeisen, K., Hillenbrand, L., & Soderblom, D. 2011, AJ, 142, 23
Foreman-Mackey, D., Agol, E., Ambikasaran, S., & Angus, R. 2017, AJ, 154, 220
Fulton, B. J., Petigura, E. A., Blunt, S., & Sinukoff, E. 2018, PASP, 130, 044504
Gaia Collaboration (Brown, A. G. A., et al.) 2018, A&A, 616, A1
Galland, F., Lagrange, A. M., Udry, S., et al. 2005a, A&A, 444, L21
Galland, F., Lagrange, A. M., Udry, S., et al. 2005b, A&A, 443, 337
Galland, F., Lagrange, A. M., Udry, S., et al. 2006, A&A, 452, 709
Gaudi, B. S., Stassun, K. G., Collins, K. A., et al. 2017, Nature, 546, 514
Gavel, D., Kupke, R., Dillon, D., et al. 2014, in Society of Photo-Optical Instrumentation Engineers (SPIE) Conference Series, Adaptive Optics Systems IV, eds. E. Marchetti, L. M. Close, & J.-P. Vran, 9148, 914805
Gillen, E., Hillenbrand, L. A., David, T. J., et al. 2017, ApJ, 849, 11
Gray, R. O., & Corbally, C. J. 1994, AJ, 107, 742
Grieves, N., Bouchy, F., Lendl, M., et al. 2021, A&A, 652, A127
Guillot, T., Abe, L., Agabi, A., et al. 2015, Astron. Nachr., 336, 638
Hennebelle, P., & Chabrier, G. 2008, ApJ, 684, 395
Hodžić, V., Triaud, A. H. M. J., Anderson, D. R., et al. 2018, MNRAS, 481, 5091
Høg, E., Fabricius, C., Makarov, V. V., et al. 2000, A&A, 355, L27
Hooton, M. J., Hoyer, S., Kitzmann, D., et al. 2022, A&A, 658, A75
Huang, C. X., Vanderburg, A., Pál, A., et al. 2020, Res. Notes Am. Astron. Soc., 4, 204
Irwin, J., Buchhave, L., Berta, Z. K., et al. 2010, ApJ, 718, 1353
Irwin, J. M., Charbonneau, D., Esquerdo, G. A., et al. 2018, AJ, 156, 140
Jackman, J. A. G., Wheatley, P. J., Bayliss, D., et al. 2019, MNRAS, 489, 5146
Jenkins, J. M., Twicken, J. D., McCauliff, S., et al. 2016, in Society of Photo-Optical Instrumentation Engineers (SPIE) Conference Series, Software and Cyberinfrastructure for Astronomy IV, eds. G. Chiozzi, & J. C. Guzman, 9913, 99133E
Jensen, E. 2013, Tapir: A web interface for transit/eclipse observability, Astrophysics Source Code Library [record ascl:1306.007]
Johnson, J. A., Apps, K., Gazak, J. Z., et al. 2011, ApJ, 730, 79
Jones, M. I., Brahm, R., Espinoza, N., et al. 2019, A&A, 625, A16
Kennedy, G. M., & Kenyon, S. J. 2008, ApJ, 673, 502
Kounkel, M., Covey, K., & Stassun, K. G. 2020, AJ, 160, 279
Kraft, R. P. 1967, ApJ, 150, 551
Kreidberg, L. 2015, PASP, 127, 1161
Kupke, R., Gavel, D., Roskosi, C., et al. 2012, in Society of Photo-Optical Instrumentation Engineers (SPIE) Conference Series, Adaptive Optics Systems III, eds. B. L. Ellerbroek, E. Marchetti, & J.-P. Véran, 8447, 84473G

Kurucz, R. L. 1992, in The Stellar Populations of Galaxies, eds. B. Barbuy & A. Renzini, 149, 225

Lagrange, A. M., Rubini, P., Nowak, M., et al. 2020, A&A, 642, A18

Li, J., Tenenbaum, P., Twicken, J. D., et al. 2019, PASP, 131, 024506

Lucy, L. B., & Sweeney, M. A. 1971, AJ, 76, 544

Ma, B., & Ge, J. 2014, MNRAS, 439, 2781

Mamajek, E. E., & Hillenbrand, L. A. 2008, ApJ, 687, 1264

Mayor, M., & Queloz, D. 1995, Nature, 378, 355

McCully, C., Volgenau, N. H., Harbeck, D.-R., et al. 2018, in Society of Photo-Optical Instrumentation Engineers (SPIE) Conference Series, Proc. SPIE, 10707, 107070K

McGurk, R., Rockosi, C., Gavel, D., et al. 2014, in Society of Photo-Optical Instrumentation Engineers (SPIE) Conference Series, Adaptive Optics Systems IV, eds. E. Marchetti, L. M. Close, & J.-P. Vran, 9148, 91483A

Mékarnia, D., Guillot, T., Rivet, J. P., et al. 2016, MNRAS, 463, 45

Miller, N., & Fortney, J. J. 2011, ApJ, 736, L29

Moutou, C., Bonomo, A. S., Bruno, G., et al. 2013, A&A, 558, A6

Nowak, G., Palle, E., Gandolfi, D., et al. 2017, AJ, 153, 131

Otegi, J. F., Bouchy, F., & Helled, R. 2020, A&A, 634, A43

Palle, E., Luque, R., Zapatero Osorio, M. R., et al. 2021, A&A, 650, A55

Paredes, L. A., Henry, T. J., Quinn, S. N., et al. 2021, AJ, 162, 176

Pepe, F., Mayor, M., Rupprecht, G., et al. 2002, The Messenger, 110, 9

Persson, C. M., Csizmadia, S., Mustill, A. e. J., et al. 2019, A&A, 628, A64

Queloz, D., Mayor, M., Udry, S., et al. 2001, The Messenger, 105, 1

Ricker, G. R., Winn, J. N., Vanderspek, R., et al. 2015, J. Astron. Telescopes Instrum. Syst., 1, 014003

Santerne, A., Fressin, F., Díaz, R. F., et al. 2013, A&A, 557, A139

Santerne, A., Moutou, C., Tsantaki, M., et al. 2016, A&A, 587, A64

Santos, N. C., Adibekyan, V., Figueira, P., et al. 2017, A&A, 603, A30

Savel, A. B., Dressing, C. D., Hirsch, L. A., et al. 2020, AJ, 160, 287

Schlaufman, K. C. 2018, ApJ, 853, 37

Schlegel, D. J., Finkbeiner, D. P., & Davis, M. 1998, ApJ, 500, 525

Sestovic, M., Demory, B.-O., & Queloz, D. 2018, A&A, 616, A76

Siverd, R. J., Beatty, T. G., Pepper, J., et al. 2012, ApJ, 761, 123

Skrutskie, M. F., Cutri, R. M., Stiening, R., et al. 2006, AJ, 131, 1163

Smith, J. C., Stumpe, M. C., Van Cleve, J. E., et al. 2012, PASP, 124, 1000

Speagle, J. S. 2020, MNRAS, 493, 3132

Stassun, K. G., & Torres, G. 2016, AJ, 152, 180

Stassun, K. G., & Torres, G. 2021, ApJ, 907, L33

Stassun, K. G., Mathieu, R. D., & Valenti, J. A. 2006, Nature, 440, 311

Stassun, K. G., Collins, K. A., & Gaudi, B. S. 2017, AJ, 153, 136

Stassun, K. G., Corsaro, E., Pepper, J. A., & Gaudi, B. S. 2018, AJ, 155, 22

Stassun, K. G., Oelkers, R. J., Paegert, M., et al. 2019, AJ, 158, 138

Stumpe, M. C., Smith, J. C., Van Cleve, J. E., et al. 2012, PASP, 124, 985

Stumpe, M. C., Smith, J. C., Catanzarite, J. H., et al. 2014, PASP, 126, 100

Talens, G. J. J., Albrecht, S., Spronck, J. F. P., et al. 2017, A&A, 606, A73

Šubjak, J., Sharma, R., Carmichael, T. W., et al. 2020, AJ, 159, 151

Temple, L. Y., Hellier, C., Albrow, M. D., et al. 2017, MNRAS, 471, 2743

Tokovinin, A. 2018, PASP, 130, 035002

Tokovinin, A., Fischer, D. A., Bonati, M., et al. 2013, PASP, 125, 1336

Torres, G., Andersen, J., & Giménez, A. 2010, A&Ar, 18, 67

Tremblin, P., Chabrier, G., Mayne, N. J., et al. 2017, ApJ, 841, 30

Triaud, A. H. M. J., Hebb, L., Anderson, D. R., et al. 2013, A&A, 549, A18

Triaud, A. H. M. J., Burgasser, A. J., Burdanov, A., et al. 2020, Nat. Astron., 4, 650

Twicken, J. D., Catanzarite, J. H., Clarke, B. D., et al. 2018, PASP, 130, 064502

Udry, S., Mayor, M., & Santos, N. C. 2003, A&A, 407, 369

Vanderburg, A., Plavchan, P., Johnson, J. A., et al. 2016, MNRAS, 459, 3565

Winn, J. N., Fabrycky, D., Albrecht, S., & Johnson, J. A. 2010, ApJ, 718, L145

Wong, I., Shporer, A., Zhou, G., et al. 2021, AJ, 162, 256

Yee, S. W., Petigura, E. A., & von Braun, K. 2017, ApJ, 836, 77

Zhou, G., Bakos, G. Á., Bayliss, D., et al. 2019, AJ, 157, 31

[1] Observatoire de Genève, Université de Genève, Chemin Pegasi, 51, 1290 Versoix, Switzerland
e-mail: angeliki.psaridi@unige.ch

[2] Vanderbilt University, Department of Physics & Astronomy, 6301 Stevenson Center Lane, Nashville, TN 37235, USA

[3] Institute for Astronomy, University of Edinburgh, Royal Observatory, Blackford Hill, Edinburgh EH9 3HJ, UK

[4] Department of Physics, University of Warwick, Gibbet Hill Road, Coventry CV4 7AL, UK

[5] Centre for Exoplanets and Habitability, University of Warwick, Gibbet Hill Road, Coventry CV4 7AL, UK

[6] Núcleo de Astronomía, Facultad de Ingeniería y Ciencias, Universidad Diego Portales, Av. Ejército 441, Santiago, Chile

[7] Department of Astronomy, Tsinghua University, Beijing 100084, PR China

[8] Department of Physics and Kavli Institute for Astrophysics and Space Research, Massachusetts Institute of Technology, Cambridge, MA 02139, USA

[9] Harvard University, Cambridge, MA 02138, USA

[10] Facultad de Ingeniería y Ciencias, Universidad Adolfo Ibáñez, Av. Diagonal las Torres 2640, Peñalolén, Santiago, Chile

[11] Millennium Institute for Astrophysics, Chile

[12] NASA Exoplanet Science Institute, Caltech/IPAC, Mail Code 100-22, 1200 E. California Blvd., Pasadena, CA 91125, USA

[13] Department of Physics and Astronomy, University of Kansas, Lawrence, KS 66045, USA

[14] Cavendish Laboratory, JJ Thomson Avenue, Cambridge CB3 0HE, UK

[15] NASA Ames Research Center, Moffett Field, CA 94035, USA

[16] University of Grenoble Alpes, CNRS, IPAG, 38000 Grenoble, France

[17] Centro de Astrofísica y Tecnologías Afines (CATA), Casilla 36-D, Santiago, Chile

[18] Center for Astrophysics, Harvard & Smithsonian, 60 Garden Street, Cambridge, MA 02138, USA

[19] Department of Physics and Astronomy, Michigan State University, East Lansing, MI 48824, USA

[20] Centre for Astrophysics, University of Southern Queensland, Toowoomba, QLD 4350, Australia

[21] Center for Astrophysics | Harvard & Smithsonian, 60 Garden Street, Cambridge, MA 02138, USA

[22] George Mason University, 4400 University Drive, Fairfax, VA 22030, USA

[23] Department of Astronomy, University of California Berkeley, Berkeley, CA 94720, USA

[24] El Sauce Observatory, Coquimbo Province, Chile

[25] Department of Physics and Astronomy, University of New Mexico, 210 Yale Blvd NE, Albuquerque, NM 87106, USA

[26] University of Zürich, Institute for Computational Science, Winterthurerstrasse 190, 8057 Zurich, Switzerland

[27] Brierfield Observatory, New South Wales, Australia

[28] NASA Goddard Space Flight Center, 8800 Greenbelt Rd, Greenbelt, MD 20771, USA

[29] Patashnick Voorheesville Observatory, Voorheesville, NY 12186, USA

[30] Kotizarovci Observatory, Sarsoni 90, 51216 Viskovo, Croatia

[31] Hazelwood Observatory, Australia

[32] Université Côte d'Azur, Observatoire de la Côte d'Azur, CNRS, Laboratoire Lagrange, Bd de l'Observatoire, CS 34229, 06304 Nice cedex 4, France

Appendix A: Light curves

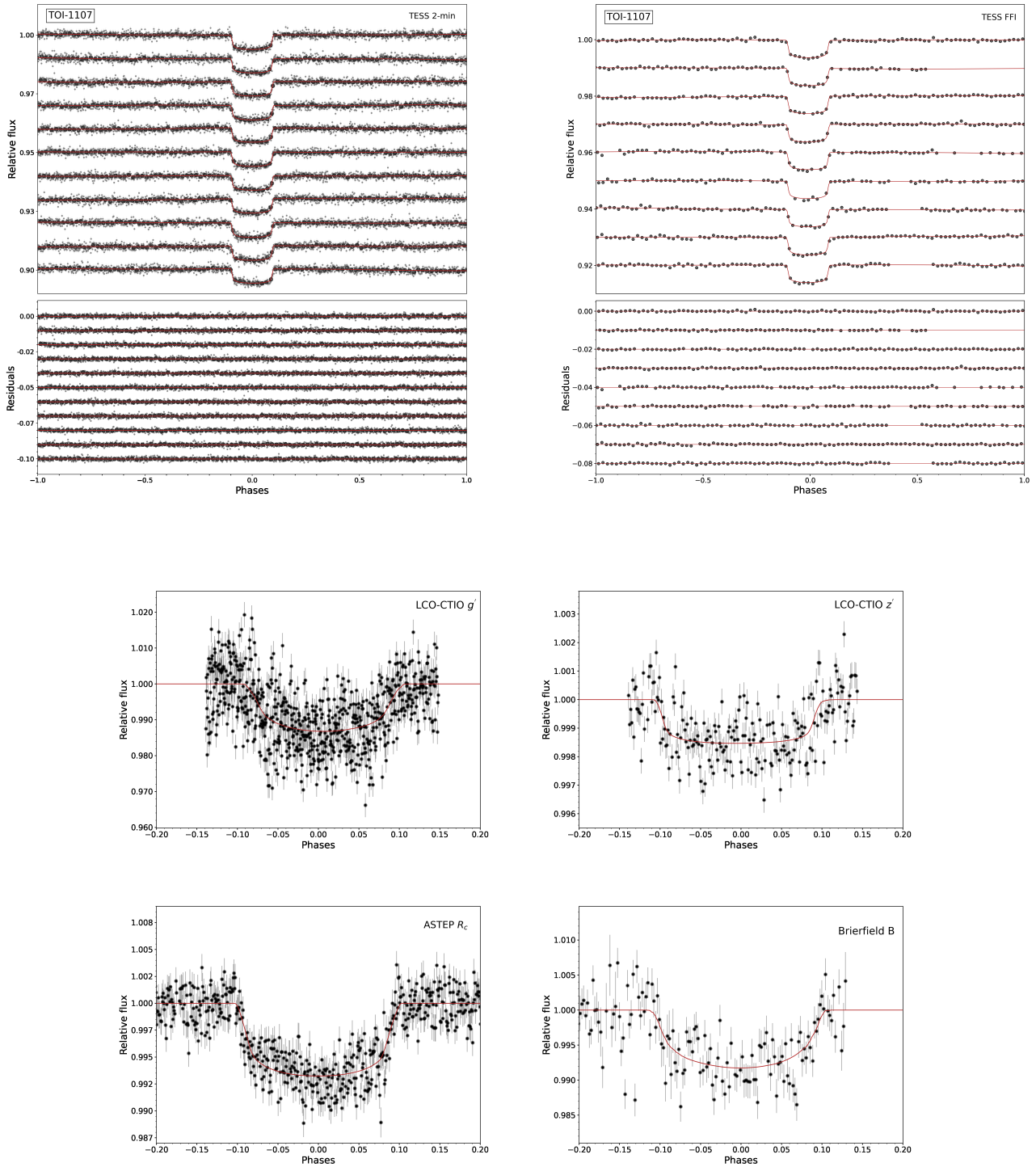Fig. A.1: TESS and ground-based light curves of TOI-1107. *Top*: TOI-1107 TESS 2-min and FFI light curves. In the 2-minute cadence light curves the observed flux is shown in light gray circles and the 30-min binned flux in black circles. The red line shows the GP and planet models that have been fit. *Bottom*: TOI-1107 detrended ground-based light curves with the best-fit linear model shown in red.
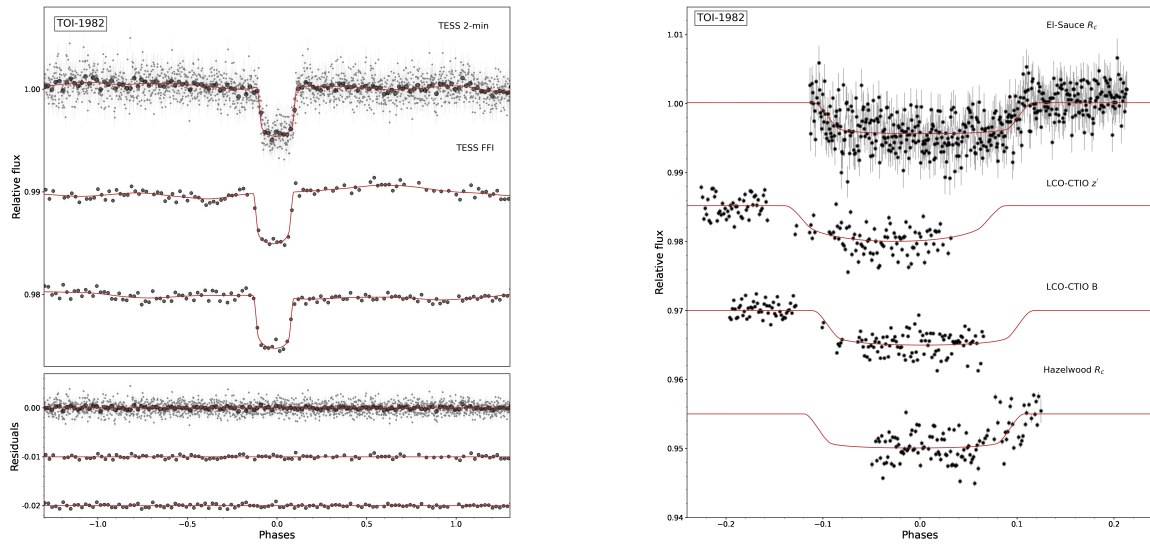
Fig. A.2: TESS and ground-based light curves of TOI-1982. *Left*: TOI-1982 TESS 2-minute and FFI light curves. In the 2-minute cadence light curves the observed flux is shown in light gray circles and the 30-minute binned flux in black circles. The red line shows the GP and planet models that have been fit. *Right*: TOI-1982 detrended ground-based light curves with the best-fit linear model shown in red.

Fig. A.3: TOI-629 TESS 2-minute and FFI light curves. In the 2-minute cadence light curves the observed flux is shown in light gray circles and the 30-minute binned flux in black circles. The red line shows the GP and planet models that have been fit.
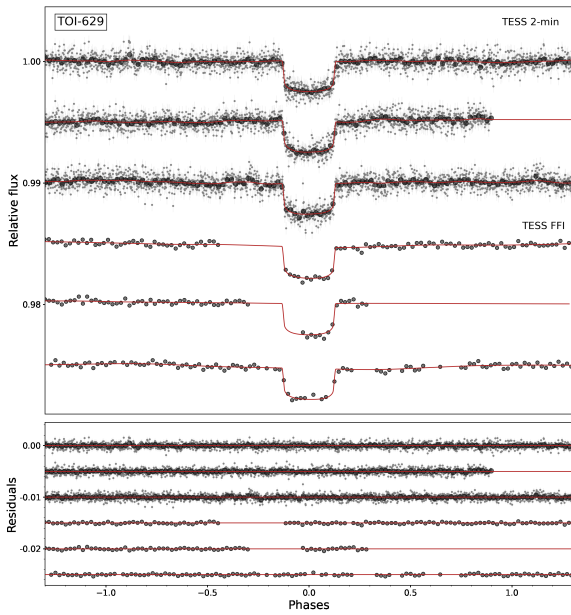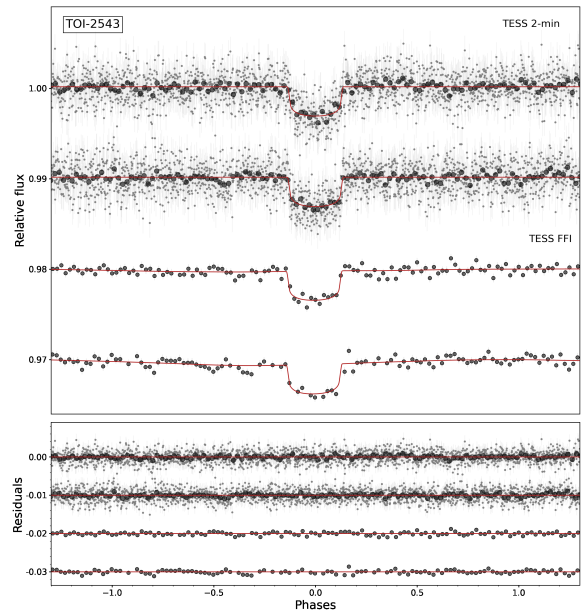

Fig. A.4: TOI-2543 TESS 2-minute and FFI light curves. In the 2-minute cadence light curves the observed flux is shown in light gray circles and the 30-minute binned flux in black circles. The red line shows the GP and planet models that have been fit.

Appendix B: Global analysis with `juliet`

Table B.1: Prior and posterior values for the joint photometric and radial velocity fit with `juliet` of TOI-629 (*left*) and TOI-2543 (*right*).

Parameter[1]	Prior[2]	Posterior estimate[3]	Parameter[1]	Prior[2]	Posterior estimate[3]
TOI-629			**TOI-2543**		
Star:			**Star:**		
ρ_* (cgs)	$\mathcal{N}(0.240, 0.031)$	$0.240^{+0.017}_{-0.022}$	ρ_* (cgs)	$\mathcal{N}(0.260, 0.030)$	$0.259^{+0.015}_{-0.022}$
Companion:			**Companion:**		
P (days)	$\mathcal{U}(8.70, 8.72)$	$8.717993^{+0.000012}_{-0.000013}$	P (days)	$\mathcal{U}(7.4, 7.7)$	$7.542776^{+0.000031}_{-0.000031}$
T_C (BJD$_{TDB}$)	$\mathcal{U}(2459204.2, 2459204.3)$	$2459204.2552^{+0.0005}_{-0.0005}$	T_C (BJD$_{TDB}$)	$\mathcal{U}(2459233.2, 2459233.5)$	$2459233.3450^{+0.0015}_{-0.0015}$
r_1	$\mathcal{U}(0, 1)$	$0.4686^{+0.0856}_{-0.0005}$	r_1	$\mathcal{U}(0, 1)$	$0.4568^{+0.0883}_{-0.0813}$
r_2	$\mathcal{U}(0, 1)$	$0.04790^{+0.00043}_{-0.00042}$	r_2	$\mathcal{U}(0, 1)$	$0.05299^{+0.00077}_{-0.00076}$
e	$\mathcal{U}(0, 1)$	$0.2986^{+0.0076}_{-0.0075}$	e	$\mathcal{U}(0, 1)$	$0.0090^{+0.0028}_{-0.0022}$
ω_* (deg)	$\mathcal{U}(0, 360)$	$8.53^{+3.05}_{-3.21}$	ω_* (deg)	$\mathcal{U}(0, 360)$	$328.1^{+19.7}_{-17.3}$
K (km s^{-1})	$\mathcal{U}(3, 5)$	$3.954^{+0.073}_{-0.072}$	K (km s^{-1})	$\mathcal{U}(4, 10)$	$6.775^{+0.029}_{-0.029}$
TESS 2-min:			**TESS 2-min:**		
$q_{1,TPF}$	$\mathcal{N}(0.180, 0.048)$	$0.207^{+0.037}_{-0.036}$	$q_{1,TPF}$	$\mathcal{N}(0.303, 0.065)$	$0.316^{+0.061}_{-0.060}$
$q_{2,TPF}$	$\mathcal{N}(0.182, 0.034)$	$0.181^{+0.036}_{-0.035}$	$q_{2,TPF}$	$\mathcal{N}(0.224, 0.027)$	$0.227^{+0.027}_{-0.027}$
D_{TPF}	$\mathcal{F}(1)$	–	D_{TPF}	$\mathcal{F}(1)$	–
M_{TPF}	$\mathcal{N}(0, 0.1)$	$(-7.16^{+1.72}_{-1.75}) \times 10^{-5}$	M_{TPF}	$\mathcal{N}(0, 0.1)$	$(-1.71^{+0.27}_{-0.26}) \times 10^{-4}$
$\sigma_{w,TPF}$ (ppm)	$\log\mathcal{U}(1, 1000)$	123^{+20}_{-25}	$\sigma_{w,TPF}$ (ppm)	$\mathcal{F}(0)$	-
$\sigma_{GP,TPF}$ (relative flux)	$\log\mathcal{U}(10^{-6}, 1)$	$(9.52^{+1.32}_{-1.17}) \times 10^{-5}$	$\sigma_{GP,TPF}$ (relative flux)	$\log\mathcal{U}(10^{-7}, 1)$	$0.305^{+0.323}_{-0.275}$
$\rho_{GP,TPF}$ (days)	$\log\mathcal{U}(0.005, 0.26)$	$0.102^{+0.040}_{-0.027}$	$\rho_{GP,TPF}$ (days)	$\log\mathcal{U}(0.0001, 3.0)$	$0.021^{+0.696}_{-0.020}$
TESS QLP:			**TESS QLP:**		
$q_{1,QLP}$	$\mathcal{N}(0.180, 0.048)$	$0.207^{+0.037}_{-0.036}$	$q_{1,QLP}$	$\mathcal{N}(0.303, 0.065)$	$0.316^{+0.061}_{-0.060}$
$q_{2,QLP}$	$\mathcal{N}(0.182, 0.034)$	$0.181^{+0.036}_{-0.035}$	$q_{2,QLP}$	$\mathcal{N}(0.224, 0.027)$	$0.227^{+0.027}_{-0.027}$
D_{QLP}	$\mathcal{F}(1)$	–	D_{QLP}	$\mathcal{F}(1)$	–
M_{QLP}	$\mathcal{N}(0, 0.1)$	$(-4.38^{+7.24}_{-7.49}) \times 10^{-5}$	M_{QLP}	$\mathcal{N}(0, 0.1)$	$(1.46^{+1.13}_{-1.26}) \times 10^{-4}$
$\sigma_{w,QLP}$ (ppm)	$\mathcal{F}(0)$	-	$\sigma_{w,QLP}$ (ppm)	$\mathcal{F}(0)$	-
$\sigma_{GP,QLP}$ (relative flux)	$\log\mathcal{U}(0.00005, 1)$	$(19.74^{+5.93}_{-4.09}) \times 10^{-5}$	$\sigma_{GP,QLP}$ (relative flux)	$\log\mathcal{U}(10^{-6}, 1)$	$(2.62^{+1.04}_{-0.70}) \times 10^{-4}$
$\rho_{GP,QLP}$ (days)	$\log\mathcal{U}(0.009, 1.6)$	$0.685^{+0.275}_{-0.192}$	$\rho_{GP,QLP}$ (days)	$\log\mathcal{U}(0.001, 2.0)$	$0.712^{+0.367}_{-0.267}$
RV:			**RV:**		
$\sigma_{w,CORALIE}$ (km s^{-1})	$\log\mathcal{U}(0.01, 0.6)$	$0.316^{+0.062}_{-0.051}$	$\sigma_{w,CORALIE}$ (km s^{-1})	$\log\mathcal{U}(0.001, 10.)$	$0.184^{+0.064}_{-0.039}$
$\mu_{CORALIE}$ (km s^{-1})	$\mathcal{U}(-13, -9)$	$-10.34^{+0.08}_{-0.07}$	$\mu_{CORALIE}$ (km s^{-1})	$\mathcal{U}(27.0, 45.0)$	$34.17^{+0.06}_{-0.07}$
$\sigma_{w,TRES}$ (km s^{-1})	$\mathcal{F}(0)$	–	$\sigma_{w,CHIRON}$ (km s^{-1})	$\mathcal{F}(0)$	-
μ_{TRES} (km s^{-1})	$\mathcal{U}(-3, 0)$	$-2.12^{+0.06}_{-0.06}$	μ_{CHIRON} (km s^{-1})	$\mathcal{U}(28, 38)$	$32.03^{+0.02}_{-0.02}$
			$\sigma_{w,TRES}$ (km s^{-1})	$\mathcal{F}(0)$	–
			μ_{TRES} (km s^{-1})	$\mathcal{U}(-10, 3)$	$-6.91^{+0.07}_{-0.07}$

Notes: [1] Parameter description: Density (ρ_*), Period (P), Time of conjunction (T_C), parametrization for p and b (r_1), parametrization for p and b (r_2), eccentricity of the orbit (e), argument of periastron (ω_*), radial-velocity semi-amplitude of the companion (K), quadratic limb-darkening parametrization (q_1), quadratic limb-darkening parametrization (q_2), dilution factor (D), offset relative flux (M), jitter added in quadrature to the errorbars σ_w, amplitude of the GP (σ_{GP}), time/length-scale of the GP (ρ_{GP}), and systemic radial velocity (μ).
[2] For the priors, $\mathcal{N}(\mu, \sigma^2)$ indicates a normal distribution with mean μ and variance σ^2, $\mathcal{U}(a, b)$ a uniform distribution between a and b, $\log\mathcal{U}(a, b)$ a log-uniform distribution between a and b and $\mathcal{F}(a)$ a parameter fixed to value a.
[3] The posterior estimate indicates the median value and then error bars the 68 % credibility intervals.

Table B.2: Prior and posterior values for the joint photometric and radial velocity fit with `juliet` of TOI-1107 (*left*) and TOI-1982 (*right*).

Parameter[1]	Prior[2]	Posterior estimate[3]	Parameter[1]	Prior[2]	Posterior estimate[3]
TOI-1107			**TOI-1982**		
Star:			**Star:**		
ρ_* (cgs)	$\mathcal{N}(0.293, 0.040)$	$0.337^{+0.024}_{-0.026}$	ρ_* (cgs)	$\mathcal{N}(0.549, 0.061)$	$0.571^{+0.048}_{-0.047}$
Companion:			**Companion:**		
P (days)	$\mathcal{U}(4.0, 4.1)$	$4.0782387^{+0.0000024}_{-0.0000025}$	P (days)	$\mathcal{U}(17.0, 17.3)$	$17.172446^{+0.000043}_{-0.000044}$
T_C (BJD$_{\rm TDB}$)	$\mathcal{U}(2459385.0, 2459385.1)$	$2459385.0123^{+0.0002}_{-0.0002}$	T_C (BJD$_{\rm TDB}$)	$\mathcal{U}(2459323.7, 2459323.9)$	$2459323.8230^{+0.0013}_{-0.0014}$
r_1	$\mathcal{U}(0, 1)$	$0.4358^{+0.0709}_{-0.0662}$	r_1	$\mathcal{U}(0, 1)$	$0.8797^{+0.0083}_{-0.0085}$
r_2	$\mathcal{U}(0, 1)$	$0.07379^{+0.00033}_{-0.00030}$	r_2	$\mathcal{U}(0, 1)$	$0.06914^{+0.00095}_{-0.00096}$
e	$\mathcal{U}(0, 1)$	$0.0247^{+0.0234}_{-0.0164}$	e	$\mathcal{U}(0, 1)$	$0.2725^{+0.0138}_{-0.0143}$
ω_* (deg)	$\mathcal{U}(0, 360)$	$71.97^{+20.48}_{-42.43}$	ω_* (deg)	$\mathcal{U}(0, 360)$	$268.15^{+1.24}_{-1.45}$
K (kms^{-1})	$\mathcal{U}(0, 1)$	$0.349^{+0.013}_{-0.013}$	K (kms^{-1})	$\mathcal{U}(0, 20)$	$4.121^{+0.073}_{-0.069}$
TESS 2-min:			**TESS 2-min:**		
$q_{1,TPF}$	$\mathcal{N}(0.306, 0.064)$	$0.219^{+0.032}_{-0.029}$	$q_{1,TPF}$	$\mathcal{N}(0.299, 0.066)$	$0.291^{+0.061}_{-0.057}$
$q_{2,TPF}$	$\mathcal{N}(0.228, 0.026)$	$0.226^{+0.025}_{-0.025}$	$q_{2,TPF}$	$\mathcal{N}(0.218, 0.027)$	$0.218^{+0.026}_{-0.027}$
M_{TPF}	$\mathcal{N}(0, 0.1)$	$(-1.30^{+0.36}_{-0.37}) \times 10^{-4}$	M_{TPF}	$\mathcal{N}(0, 0.1)$	$(-2.33^{+1.13}_{-1.12}) \times 10^{-4}$
$\sigma_{w,TPF}$ (ppm)	$\log\mathcal{U}(10^{-4}, 1000)$	$89.38^{+34.61}_{-26.09}$	$\sigma_{w,TPF}$ (ppm)	$\mathcal{F}(0)$	–
$\sigma_{GP,TPF}$ (relative flux)	$\log\mathcal{U}(10^{-6}, 10^{-3})$	$(2.30^{+0.23}_{-0.19}) \times 10^{-4}$	$\sigma_{GP,TPF}$ (relative flux)	$\log\mathcal{U}(1, 6) \times 10^{-4}$	$(2.98^{+0.87}_{-0.62}) \times 10^{-4}$
$\rho_{GP,TPF}$ (days)	$\log\mathcal{U}(0.1, 1)$	$0.435^{+0.071}_{-0.060}$	$\rho_{GP,TPF}$ (days)	$\log\mathcal{U}(0.01, 1)$	$0.205^{+0.086}_{-0.060}$
TESS QLP:			**TESS QLP:**		
$q_{1,QLP}$	$\mathcal{N}(0.306, 0.064)$	$0.219^{+0.032}_{-0.029}$	$q_{1,QLP}$	$\mathcal{N}(0.299, 0.066)$	$0.291^{+0.061}_{-0.057}$
$q_{2,QLP}$	$\mathcal{N}(0.228, 0.026)$	$0.226^{+0.025}_{-0.025}$	$q_{2,QLP}$	$\mathcal{N}(0.218, 0.027)$	$0.218^{+0.026}_{-0.027}$
M_{QLP}	$\mathcal{N}(0, 0.1)$	$(1.35^{+4.87}_{-4.65}) \times 10^{-5}$	M_{QLP}	$\mathcal{N}(0, 0.1)$	$(1.0624^{+1.08}_{-1.10}) \times 10^{-4}$
$\sigma_{w,QLP}$ (ppm)	$\mathcal{F}(0)$	-	$\sigma_{w,QLP}$ (ppm)	$\mathcal{F}(0)$	-
$\sigma_{GP,QLP}$ (relative flux)	$\log\mathcal{U}(10^{-4}, 0.1)$	$(2.54^{+0.34}_{-0.27}) \times 10^{-4}$	$\sigma_{GP,QLP}$ (relative flux)	$\log\mathcal{U}(2, 5) \times 10^{-4}$	$(3.37^{+0.73}_{-0.57}) \times 10^{-4}$
$\rho_{GP,QLP}$ (days)	$\log\mathcal{U}(0.1, 1)$	$0.511^{+0.110}_{-0.072}$	$\rho_{GP,QLP}$ (days)	$\log\mathcal{U}(0.1, 0.5)$	$0.299^{+0.093}_{-0.077}$
ASTEP R_c:			**Hazelwood R_c:**		
$q_{1,ASTEP}$	$\mathcal{F}(0.3233)$	-	$q_{1,Hazelwood}$	$\mathcal{F}(0.12601)$	-
$q_{2,ASTEP}$	$\mathcal{F}(0.2987)$	-	$q_{2,Hazelwood}$	$\mathcal{F}(0.05544)$	-
M_{ASTEP}	$\mathcal{N}(0, 0.1)$	$0.815^{+0.294}_{-0.215}$	$M_{Hazelwood}$	$\mathcal{N}(0, 0.1)$	$(-2.73^{+1.08}_{-1.08}) \times 10^{-3}$
$\sigma_{w,ASTEP}$ (ppm)	$\log\mathcal{U}(0, 3000)$	1021^{+76}_{-75}	$\sigma_{w,Hazelwood}$ (ppm)	$\log\mathcal{U}(1900, 3000)$	2497^{+175}_{-155}
LCO-CTIO$_Z$:			**El Sauce R_c:**		
q_{1,LCO_z}	$\mathcal{F}(0.1849)$	–	$q_{1,El-Sauce}$	$\mathcal{F}(0.12601)$	-
q_{2,LCO_z}	$\mathcal{F}(0.2921)$	–	$q_{2,El-Sauce}$	$\mathcal{F}(0.05544)$	–
M_{LCO_z}	$\mathcal{N}(0, 0.1)$	$1.978^{+0.004}_{-0.004}$	$M_{El-Sauce}$	$\mathcal{N}(0, 0.1)$	$0.093^{+0.002}_{-0.002}$
σ_{w,LCO_z} (ppm)	$\log\mathcal{U}(0, 2000)$	713^{+51}_{-53}	$\sigma_{w,El-Sauce}$ (ppm)	$\mathcal{F}(0)$	-
Brierfield B:			**LCO-CTIO$_b$:**		
$q_{1,Brierfield}$	$\mathcal{F}(0.5976)$	-	q_{1,LCO_b}	$\mathcal{F}(0.61536)$	-
$q_{2,Brierfield}$	$\mathcal{F}(0.1935)$	-	q_{2,LCO_b}	$\mathcal{F}(0.35447)$	–
$M_{Brierfield}$	$\mathcal{N}(0, 0.1)$	$(-5.86^{+2.20}_{-1.94}) \times 10^2$	M_{LCO_b}	$\mathcal{N}(0, 0.1)$	$(-3.74^{+2.68}_{-2.53}) \times 10^{-3}$
$\sigma_{w,Brierfield}$ (ppm)	$\log\mathcal{U}(0, 4000)$	2514^{+281}_{-275}	σ_{w,LCO_b} (ppm)	$\log\mathcal{U}(1000, 2400)$	1895^{+124}_{-110}
LCO-CTIO$_g$:			**LCO-CTIO$_Z$:**		
q_{1,LCO_g}	$\mathcal{F}(0.535962)$	–	q_{1,LCO_z}	$\mathcal{F}(0.22016)$	–
q_{2,LCO_g}	$\mathcal{F}(0.218820)$	–	q_{2,LCO_z}	$\mathcal{F}(0.18173)$	–
M_{LCO_g}	$\mathcal{N}(0, 0.1)$	$(2.33^{+3.21}_{-3.17}) \times 10^2$	M_{LCO_z}	$\mathcal{N}(0, 0.1)$	$(-8.70^{+6.14}_{-6.39}) \times 10^{-4}$
σ_{w,LCO_g} (ppm)	$\log\mathcal{U}(0, 8000)$	6353^{+219}_{-208}	σ_{w,LCO_z} (ppm)	$\log\mathcal{U}(1000, 3000)$	1480^{+94}_{-84}
D_{All}[4]	$\mathcal{F}(1)$	–	D_{All}[4]	$\mathcal{F}(1)$	–
RV:			**RV:**		
$\sigma_{w,CORALIE}$ (km s^{-1})	$\mathcal{F}(0)$	–	$\sigma_{w,CORALIE}$ (km s^{-1})	$\log\mathcal{U}(0.001, 2)$	$0.170^{+0.057}_{-0.047}$
$\mu_{CORALIE}$ (km s^{-1})	$\mathcal{U}(40, 42)$	$40.81^{+0.01}_{-0.01}$	$\mu_{CORALIE}$ (km s^{-1})	$\mathcal{U}(-46, -20)$	$-37.74^{+0.06}_{-0.06}$
$\sigma_{w,CHIRON}$ (km s^{-1})	$\log\mathcal{U}(0.001, 1)$	$0.046^{+0.016}_{-0.012}$	$\sigma_{w,FEROS}$ (km s^{-1})	$\mathcal{F}(0)$	-
μ_{CHIRON} (km s^{-1})	$\mathcal{U}(-3, 1)$	$0.024^{+0.016}_{-0.015}$	μ_{FEROS} (km s^{-1})	$\mathcal{U}(-45, -20)$	$-37.00^{+0.13}_{-0.14}$
$\sigma_{w,MINERVA}$ (km s^{-1})	$\mathcal{F}(0)$	–	$\sigma_{w,TRES}$ (km s^{-1})	$\mathcal{F}(0)$	–
$\mu_{MINERVA}$ (km s^{-1})	$\mathcal{U}(39, 41)$	$40.19^{+0.02}_{-0.02}$	μ_{TRES} (km s^{-1})	$\mathcal{U}(-7, 8)$	$-0.113^{+0.211}_{-0.210}$

Notes: The description of [1], [2] and [3] can be found in Table B.1.
[4] The dilution factor was fixed to 1 for all the photometric data (D_{All}).

Appendix C: Spectroscopic binaries

Parameters	TOI-288 (TIC 47316976)	TOI-446 (TIC 1449640)	TOI-478 (TIC 172464366)	TOI-764 (TIC 181159386)
M_2 (M_{Jup})	332.4 ± 41.8	178.8 ± 17.3	155.6 ± 12.0	264.3 ± 9.6
R_2 (R_{Jup})	–	1.77 ± 0.15	1.78 ± 0.22	1.73 ± 0.20
P (days)	79.081	3.502	2.922	5.632
K (km s^{-1})	13.047 ± 0.886	18.331 ± 0.459	16.861 ± 0.616	22.269 ± 0.175
D (mmag)	–	16.829	17.493	13.556
ecc	0.655 ± 0.010	0.039 ± 0.027	0.004 ± 0.009	0.175 ± 0.009
M_1 ($M_\odot$)	1.38 ± 0.08	1.31 ± 0.08	1.30 ± 0.08	1.36 ± 0.08
R_1 ($R_\odot$)	1.86 ± 0.18	1.46 ± 0.18	1.44 ± 0.18	1.59 ± 0.18
T_{eff} (K)	6380 ± 110	6477 ± 110	6452 ± 110	6557 ± 110

Table C.1: List of Single lined spectral Binary (SB1) systems detected with CORALIE spectrograph.

Notes: Parameters of the primary star are noted with $_1$ and of the secondary star with $_2$ (Sect. 4.6).
Parameter description: Stellar mass ($M_{1,2}$), stellar radius ($R_{1,2}$), orbital period (P), RV semi-amplitude (K), depth (D), eccentricity (e), and primary stellar effective temperature (T_{eff}).
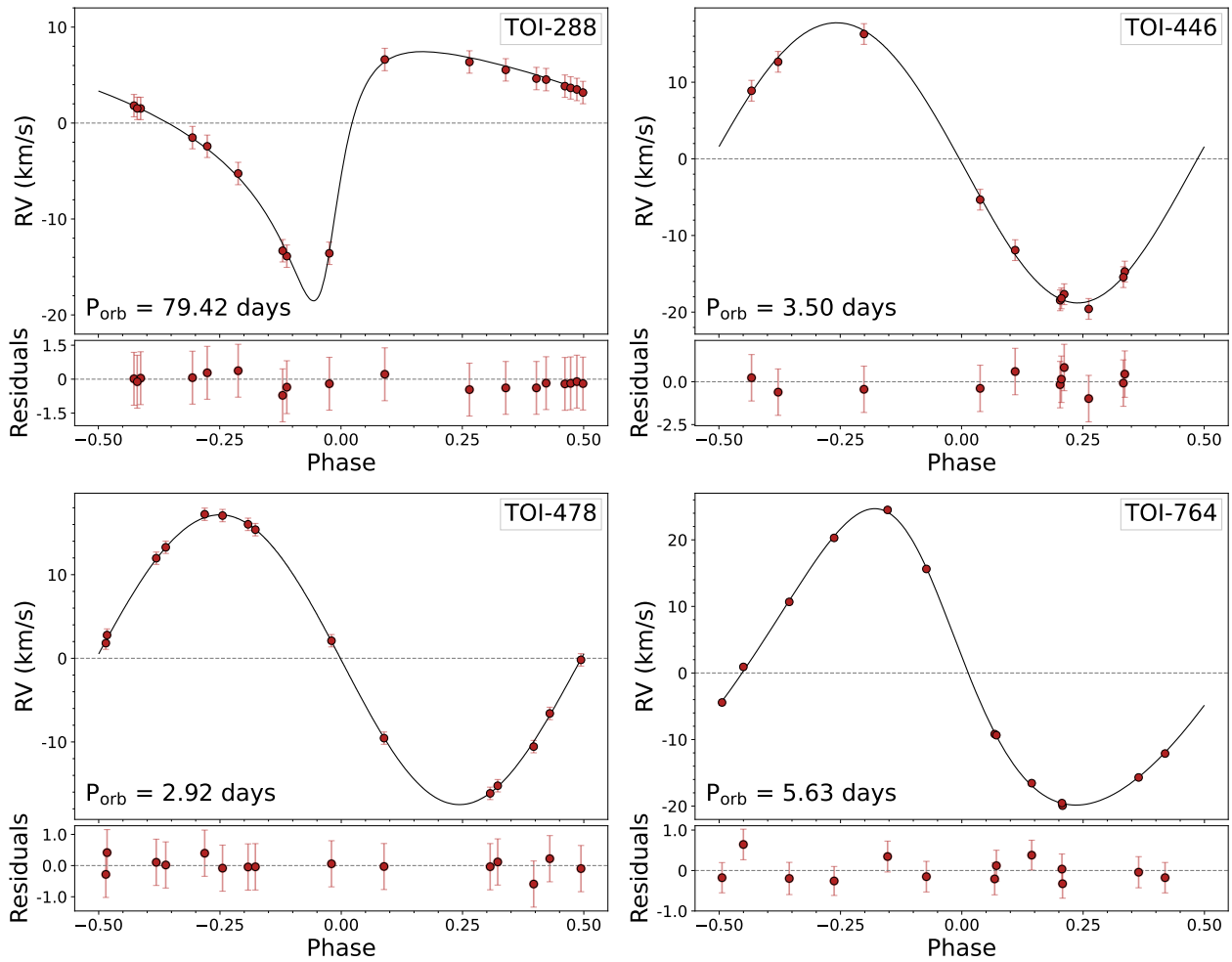

Fig. C.1: Phase-folded radial velocities of TOI-288, TOI-446, TOI-478, and TOI-764. The black line displays the model fit derived with `juliet`. The residuals of the model fit are shown in the bottom panels.